1 The T0 Detector

1.1 Naming Convention

Practically all the drawings of the ALICE detectors, starting from the early conceptual studies pre-dating the first ALICE Technical Proposal [1] until the most recent ALICE internal notes, show the detector from the same side: the muon absorber is depicted on the right-hand side of the figure (see Fig. **??**). This resulted in widespread reference to the side occupied by the muon absorber (RB26) as the RIGHT side. Consequently the opposite side (RB24) became the LEFT. The orientation of the z-axis followed the usual convention (from left to right), pointing from the interaction point to the absorber. A change of convention occurred in 2003 [2, 3]. According to the new convention the z-axis now runs in the opposite direction (right to left on all depiction of ALICE) and A, B and C are to be used to indicate detector sides. Table 1.1 clarifies the naming convention change. As far as pseudorapidity is concerned, only the absolute value $|\eta|$ will be used. This will avoid any potential problems in cross-reference to previous publications.

Table 1.1: Conversion between the old and new naming conventions for T0 detector components.

Location	Old Name	New Name
RB24 *(opposite the muon absorber)*	**T0-Left**	**T0-A**
RB26 *(on the side of the muon absorber)*	**T0-Right**	**T0-C**

1.2 Physics Objectives

The T0 detector is required to fulfil the following functions:

1. To supply main signals to the ALICE L0 trigger.
2. To deliver an early (prior to the L0 trigger) “wake–up” trigger to the TRD.
3. To give a start signal with good time resolution for the Time–of–Flight (TOF) particle identification system in ALICE.

The trigger functions requested from T0 are as follows:

- to measure the approximate vertex position;
- to give a rough estimate of event multiplicity;
- to inform that at least one of the arms of the T0 detector has registered a valid pulse.

The first trigger function is crucial for discriminating against beam–gas interactions. With 50 ps time resolution one should obtain ±1.5 cm accuracy in vertex determination. If the vertex position falls within the pre–defined values, an L0 trigger signal called *T0–vertex* will be produced.

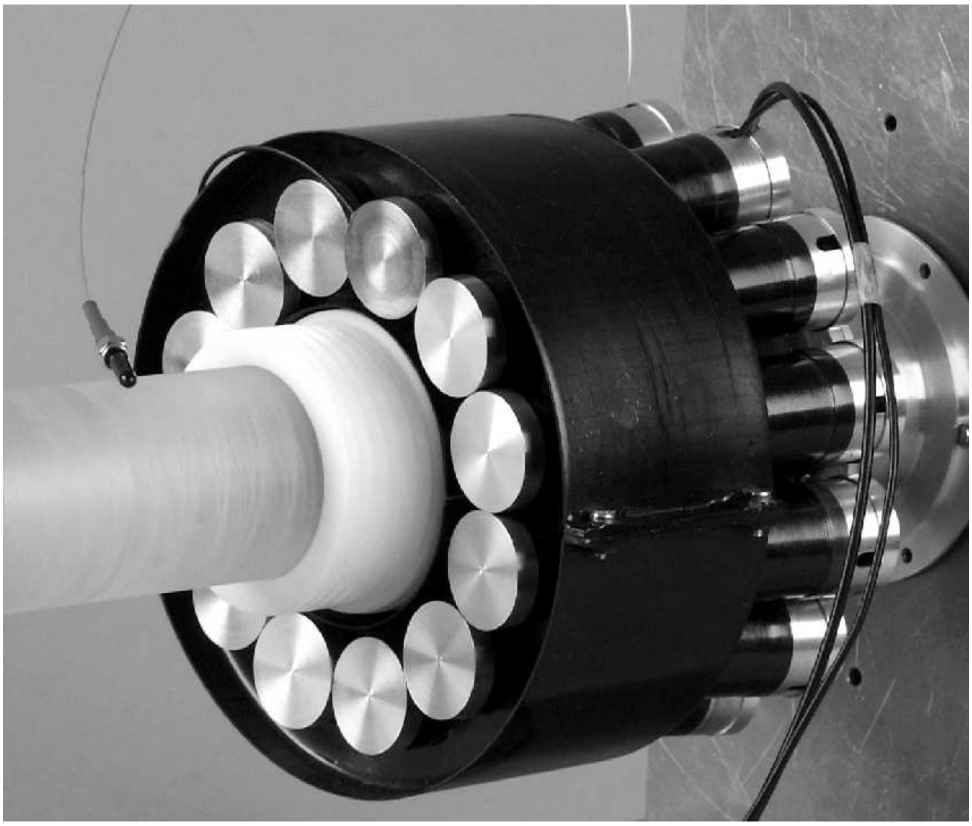

Figure 1.1: Photography of the prototype of T0-C.

The second feature (multiplicity determination) will be an important back–up option for V0 that covers a considerably larger pseudorapidity range. For T0, the covered pseudorapidity range is $2.9 < |\eta| < 3.3$ on the RB26 and $4.5 < |\eta| < 5$ on the RB24. The measured multiplicity will be compared to 2 pre–set values to generate one of the three possible trigger signals: *T0(minimum bias)*, *T0(semi–central)*, or *T0(central)*, corresponding to low, intermediate, and high multiplicities. There will be only two threshold values because the minimum bias signal is identical to *T0–vertex* (sufficient multiplicity to have triggered both halves of the T0 detector). Since the T0 detector generates the earliest L0 trigger signals, all these signals should be strictly generated on–line without the possibility of any off–line corrections.

The early wake–up signal to the Transition Radiation Detector also must be strictly produced on–line. The full list of trigger signals delivered by T0 is listed in Table 1.2.

The T0 detector is the only ALICE sub–detector capable of delivering a high–precision start signal for the TOF detector. This T0 signal must correspond to the real time of the collision (plus a fixed time delay) and be independent of the position of the vertex. The required precision of the T0 signal must be better or at least equal to that of the TOF detector ($\sigma = 50\,\text{ps}$). Generating the T0 start will not be done by any other detector in ALICE so the quality of the T0 time resolution will directly influence the quality of TOF identification. In favourable cases, mostly for HI collisions, one may expect some further improvement of T0 time resolution in off–line analysis. For that purpose it is important to read out and store the time and amplitude of each PMT of the T0 array (see the prototype of T0-C in Fig. 1.1).

1.3 Design Considerations

The requirement to generate the *T0–vertex* pulse for the ALICE trigger and to give an on–line position–independent T0–start signal implies a two–arm design with detectors on each side of the interaction

Table 1.2: List of trigger signals delivered by the T0 detector to the Central Trigger Processor (CTP) and the Transition Radiation Detector (TRD).

Trigger signal	**Purpose**	**Adjustable parameters**[1]
T0–vertex	*Beam gas suppression*; Will also serve as *minimum bias*; *Can not* be used to study *beam gas interactions* because Cherenkov detectors are direction sensitive.	*Two programmable thresholds* defining the upper and lower limit for the acceptable time difference in arrival time between T0-C and T0-A. The maximum acceptable range is about ±80 cm.
T0-C(T0-Right)	Useless as stand–alone. To be combined with V0	None
T0-A(T0-Left)	Useless as stand–alone. To be combined with V0	None
T0 semi–central	*Semi–central collisions* (back–up for V0)	*One:* threshold level
T0–central	*Central collisions* (back–up for V0)	*One:* threshold level
TRD wake–up	*Wake–up call*	*None* (There will be 24 delays and 24 thresholds to be adjusted jointly by the T0 and TRD group using laser calibration before each run.)

point. The presence of the muon absorber on the RB26 side of ALICE reduces the available space in that area to a small volume around the beam pipe, to be shared by T0, V0 and FMD. The distance from the interaction point is less than 1 m and there will be no access to that area unless the entire central part of ALICE is disassembled. All in all, only a small detector system could be considered: it must be based on well–tested and reliable technology, capable of maintenance–free operation for at least 10 years.

The total dead time of the detector, including pulse generation and processing, should be less than the bunch–crossing period in pp collisions, that is, less than 25 ns. The detector must tolerate operation inside the L3 magnet in a magnetic field of strength up to 0.5 T.

The list of design considerations can be summarised as follows:

- detectors on both sides of the interaction point
- compact design
- time resolution of about 50 ps;
- high efficiency;
- total dead time of less than 25 ns;
- operation in a magnetic field of up to 0.5 T;
- radiation tolerance up to 500 krad;
- reasonable multiplicity resolution for charged particles;
- high reliability;
- maintenance–free operation.

1.4 T0 Detector Overview

All in all, three different techniques were considered and tested for the T0 detector design: microchannel plate detectors (MCP), resistive plate chambers (RPC) and Cherenkov radiators optically coupled to photomultiplier tubes (PMT). The most ambitious and challenging of the tested alternatives was based on MCP [4, 5]. If such a detector operates properly and if it covers sufficient pseudorapidity range it will work not only as T0 but also as V0 and FMD. In other words, it will combine the functions of all 3 forward detectors in one. Unfortunately MCP technology is also the most expensive, requires operation in good vacuum and has not been used before in similar applications. Therefore, considering the available time, manpower and resources as well as proven performance, the ALICE collaboration approved in spring 2001 the PMT solution as the baseline for the T0 detector.

1.4.1 Detector Module Design

Once the PMT technology was chosen, remaining issues included the right tubes, selection of Cherenkov radiators and design the electronics. In this we could learn from the experience of the PHENIX experiment at RHIC, where a very similar detector, based on quartz radiators and Hamamatsu fine–mesh phototubes, has been built and is operated by the Hiroshima group [6]. This group, using 1.6 GeV/c negative pions, has demonstrated a time resolution of 50 ps after off–line pulse shape correction. A 100 ps resolution was obtained without any off–line correction with a simple leading–edge discriminator.

1.4.2 Photomultiplier Tube (PMT)

Currently there are only two manufacturers in the world producing PMTs capable of operation in a magnetic field and fulfilling T0 specifications. The tubes are *R5506* from the Japanese company Hamamatsu (PHENIX's choice) and *FEU–187* from the Russian firm ”Electron”. Both products are fine–mesh phototubes with good timing properties, UV entrance windows, which can operate in the axial magnetic field of 0.5 T.

In a series of extensive tests we have verified that the differences in performance between the R5506 and the FEU–187 are negligible, while the spread in key characteristic parameters of units delivered by the manufacturer in the same batch are very big. For instance, Hamamatsu's catalogue quotes anode sensitivity of 40 μA/Lm, but the actual value can be anywhere from 5 to 300. To produce a detector array giving 50 ps time resolution for any combination of the firing PMTs, they must all match closely. Ordering closely matched tubes sharply increases the price and requires good – preferably direct – contact with the producer, so that user can verify the units selected. Since we have no access to the Hamamatsu plant, but we do have good contacts with ”Electron”, we decided to use FEU–187 (presented in Fig. 1.2).

The additional factor in support of our choice was the price (even an unselected R5506 is twice as expensive as FEU–187). As a precaution the tubes in our design will be interchangeable. This means that if the need arises the change from FEU–187 to R5506 will be possible with only minimal modifications.

1.4.3 Cherenkov Radiator

It is uncertain whether a fast scintillator will survive 10 years of operation under LHC conditions, since most organic materials quickly lose transparency, especially at short wavelengths when they are exposed to high radiation doses. For these reasons we have opted for Cherenkov detectors with fused quartz radiators. Quartz is known to be radiation hard and is transparent to UV. The other advantage of the Cherenkov option is a very fast light emission in comparison with other fast scintillators.

The length of the quartz radiator was estimated based on the assumption that the PMT will respond to the 200-550 nm band of the Cherenkov light emission spectrum — see Fig. 1.3.

The average number of emitted photons per 1 cm of radiator is given by the expression:

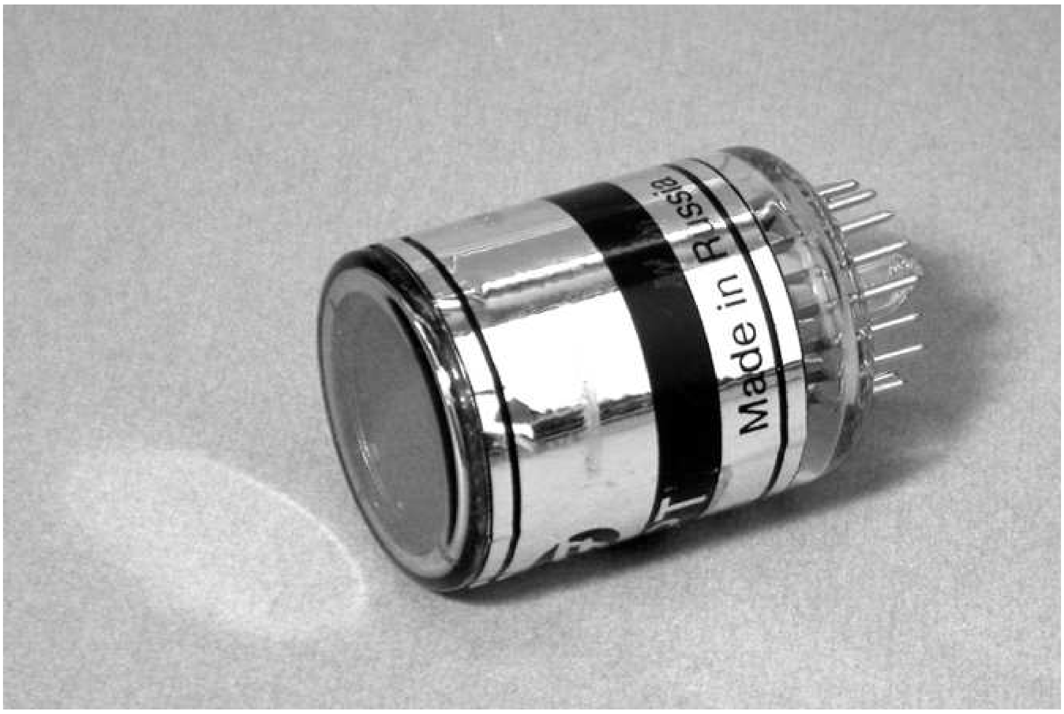

Figure 1.2: FEU–187. The outside diameter of the photomultiplier tube is 30 mm.

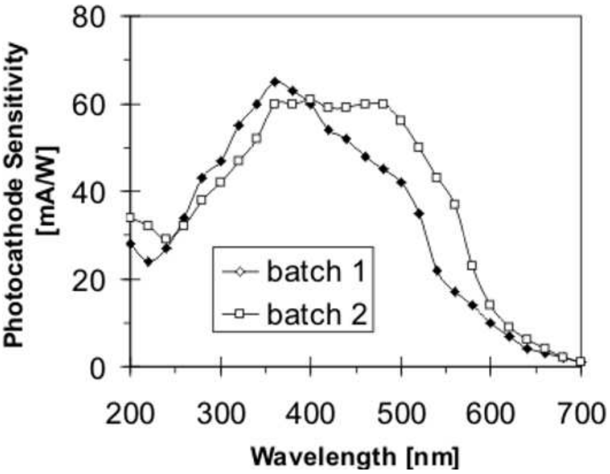

Figure 1.3: Photocathode sensitivity measured for two different production batches of FEU–187 photomultiplier tube.

$$N_{ph} = 2\pi\alpha\,(1/\lambda_2 - 1/\lambda_1)\sin^2\Theta\,. \tag{1.1}$$

For fused quartz the refraction index is $n = 1.458$, yielding $\cos\Theta = 1/n = 0.686$, $\sin^2\Theta = 0.53$. Hence the average number of photons per 1 cm length will be about 770, 440 and 250 for the wavelength bands 200-550 nm, 300-550 nm, and 350-550 nm, respectively. With these values, assuming an average quantum efficiency of the photocathode equal to 15%, we estimate 112, 66, and 38 emitted photoelectrons for the corresponding wavelength bands for a 1 cm long radiator. To triple the number of photoelectrons one needs a 3 cm long quartz radiator. According to the actual experimental data given in [6], Hamamatsu R5505 with a conventional borosilicate glass entrance window (spectral sensitivity 300-550 nm) or R5506 with a UV glass entrance window (spectral sensitivity 200-550 nm) should give enough photoelectrons to achieve a 50 ps time resolution for the very short and well–focused Cherenkov light emission. We have verified this with our own measurements of the time resolution and dynamic range of the three types of PMTs: Hamamatsu R3432–01 (which is quite similar to R5505), Hamamatsu R5506 and FEU–187.

All tests and calculations indicate that a 3 cm long quartz is a good choice for the Cherenkov radiators of the ALICE T0 detector.

1.4.4 Location and Size of the Two T0 Arrays

To measure the exact time of an event and the vertex position along the z–axis, the T0 detector should consist of two arrays of Cherenkov counters with the IP in–between. On the muon absorber side (RB26) the distance of the array from the IP is limited by the position of the absorber nose. The distance from the IP to T0-C is 70 cm – as close as possible to the absorber. On the opposite side (RB24) the distance from T0-A to the IP is about 3.6 m. T0-C covers the pseudorapidity range $2.9 < |\eta| < 3.3$, and T0-A of $4.5 < |\eta| < 5$. The chosen location of the two T0 arrays inside ALICE is shown schematically in Fig. 1.4.

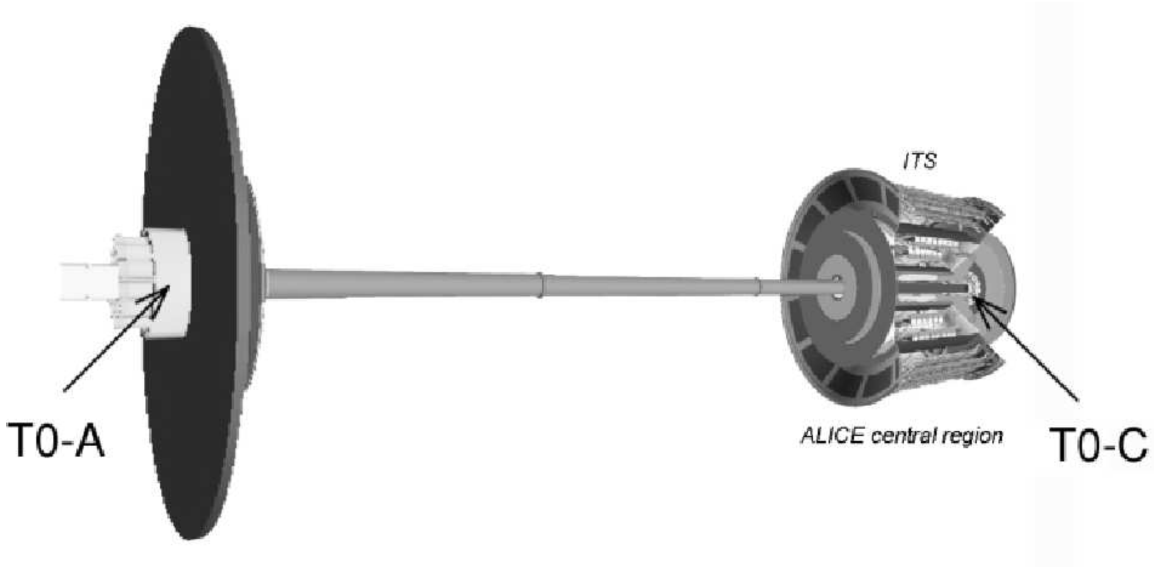

Figure 1.4: Position of the T0 detector inside ALICE.

We have made Monte Carlo simulations of the efficiency and background conditions for this geometry using the latest version of PYTHIA [6.125]. We have included Cherenkov light emission and light collection processes in the simulation procedure. Figure 1.5 shows the resulting track multiplicity for charged particles and gammas for simulated pp collisions (light grey). The y–axis shows the number of generated PYTHIA events for the given multiplicity in the range $|\eta| < 10$. If in the simulated event at least one track produced at least one photon reaching the photo cathode of a PMT in the studied array, we considered it as registered (hit) and the event was plotted in black. T0-C hits are shown in Fig. 1.5 (top), T0-A in Fig. 1.5 (bottom), and coincidence hits from the same event in both arrays are shown in Fig. 1.6.

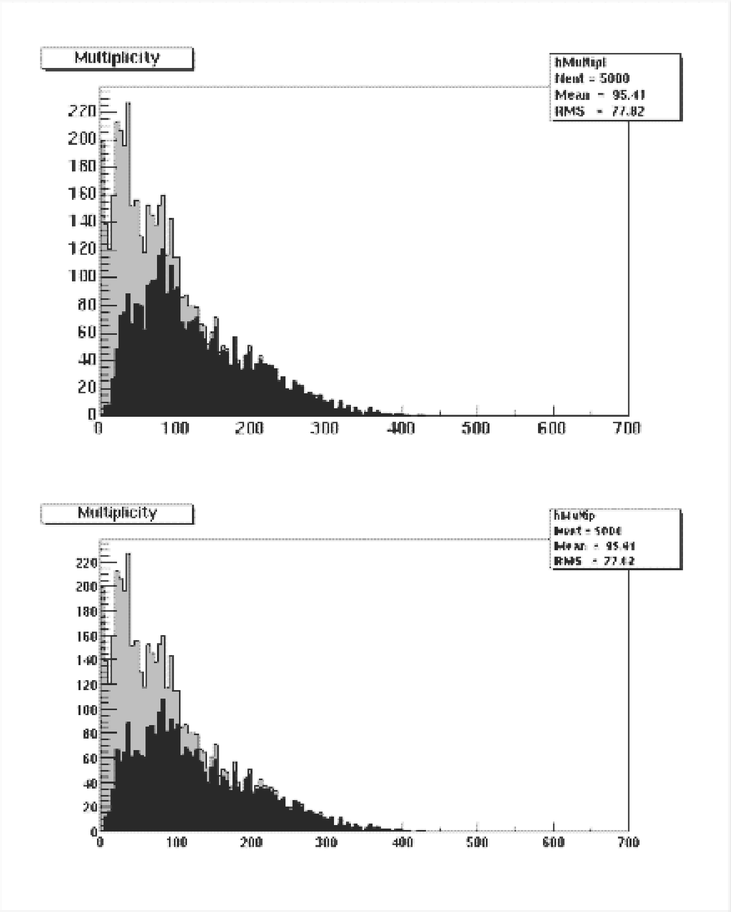

Figure 1.5: Total track multiplicity distribution of charged and neutral particles given by PYTHIA 6.125. Light grey: all events, black: those registered by T0-C (top), by the T0-A (bottom).

One can see that efficiency increases rapidly with the multiplicity of events. It becomes quite satisfactory already at $M > 100$. The combined geometrical efficiency for all processes included in PYTHIA and estimated from these distributions is about 64% for T0-C, 59 % for T0-A, and 45% for the coincidence of both arrays. The actual efficiencies should, in fact, be slightly higher (67%, 60% and 48%) due to photon conversion into electrons in the beam pipe and other material between the IP and the Cherenkov radiators. In heavy–ion collisions, with the exception of extremely peripheral collisions, the efficiency of T0 is always 100%.

The simulations were made assuming that the diameter of the Cherenkov radiators matches that of the outside diameter of the PMT (3 cm for FEU–187). By reducing the diameter one reduces the efficiency correspondingly, but gains slightly in the time resolution. This is because the active area of the photocathode is only 20 mm in diameter. At the moment 20 mm is the baseline for the radiator diameter (see Section 1.9.2).

Initially two design options were considered for the T0 array: a smaller version, with just 12 detectors in each array forming a single layer of PM tubes wrapped around the beam pipe, and a version with 24 detectors arranged in 2 layers. Due to the space constraints on the muon absorber side the smaller version was chosen. In fact simulations indicate that, unlike on the RB24 side, the second layer on the RB26 would not considerably improve efficiency as it would already be too far away ($|\eta| < 2.9$). The described calculations were made for the adopted version ($12 + 12$).

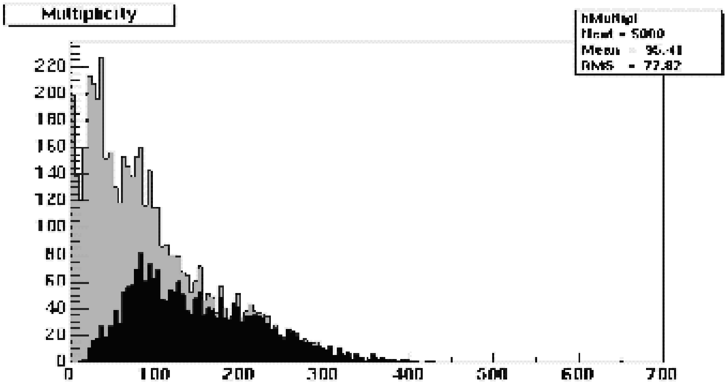

Figure 1.6: Total track multiplicity distribution of charged and neutral particles given by PYTHIA [6.125]. Light gray: all events, black: those registered by both arrays in coincidence.

1.4.5 Laser Calibration System (LCS)

The goal of the LCS is to tune the T0 electronics and monitor the performance of the detector before and during the ALICE experiments. For that reason it is necessary to provide simultaneous light pulses with adjustable amplitudes for all 24 PMTs of the T0 detector. It is highly desirable that the amplitudes of the laser pulses at the input of each PMT cover the full dynamic range of the detector and that the wavelength is well within the sensitivity range of the photocathode. Regrettably, the latter requirement excludes red lasers, which are widely used for instance in telecommunication, and therefore have a very broad range of relatively inexpensive accessories. We have only been able to find one laser that matched our specifications and price range. It is Picosecond Injection Laser PIL040G 408 nm (Fig. 1.7). The maximum power of this laser is close to the limit of that required by our application, therefore it is essential to minimize signal loss along the optical wire and couplings. It is also important that the timing characteristics of the laser pulse should be preserved on the way to the PMT. Otherwise it would be impossible to tune the arrays to better than 50 ps accuracy.

Figure 1.7: PIL040G 408 nm laser.

Tests made with the laser and 20 m long multi–mode optical fibre indicate that the LCS concept sketched in Fig. 1.8 is sound and can be used for T0 calibration. The achieved time resolution for different light outputs is plotted in Fig. 1.9. For the test a manual attenuator was used. In the actual set-up it will be replaced by a computer controlled attenuator (for instance Digital Variable Attenuator `DA--100--3S--830--9/125--M--3`) [12]. The attenuated signal will then be split into 24 identical

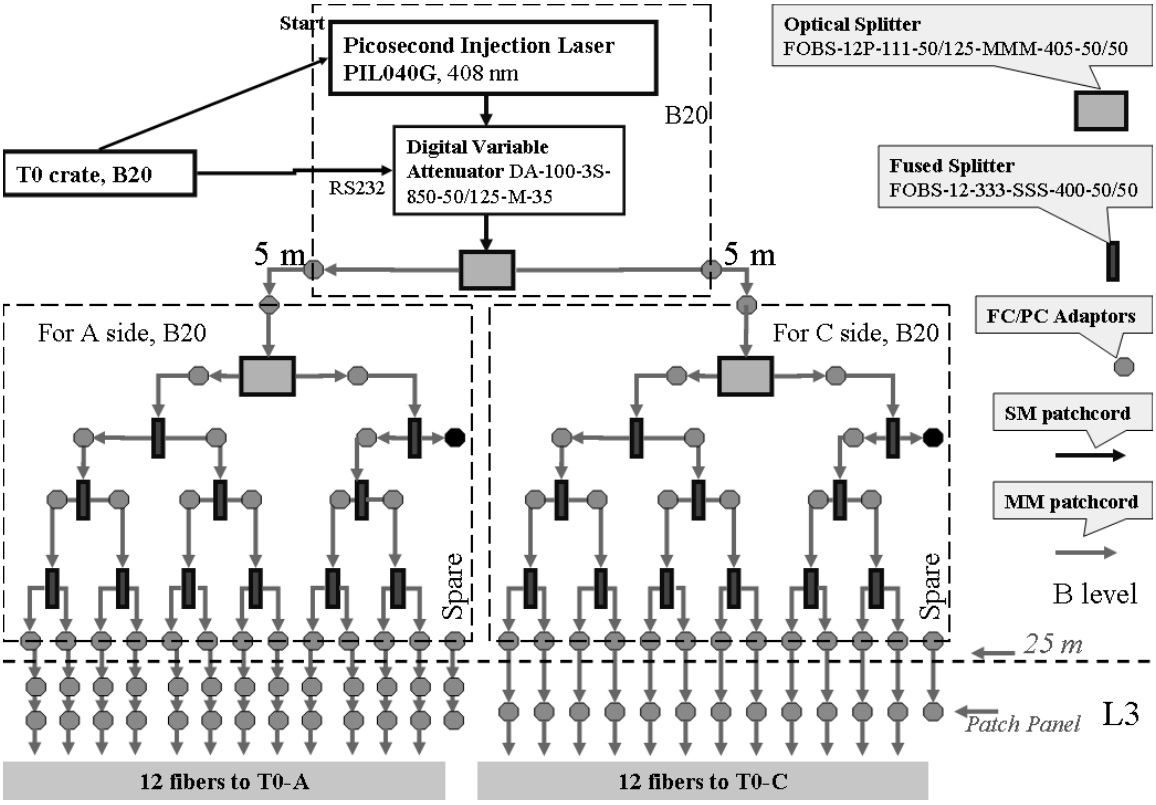

Figure 1.8: Current conceptual drawing of LCS.

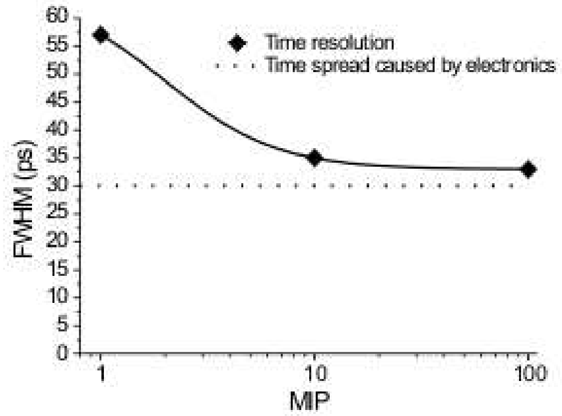

Figure 1.9: Time resolution measured with laser amplitudes corresponding to 1, 10 and 100 MIP. The laser pulse was delivered over 20 m of multi–mode optical fibre. The resolution coming from the electronic noise is also plotted.

pulses and delivered to 24 PMT arrays, about 25 m from the laser. The PMTs will be divided into 2 groups of 12 PMTs and placed in different locations. Each PMT will be equipped with a short (1 m) optical fibre. One end of this fibre will have a standard connector to couple to the 25 m fibre coming from the laser. The other end will be permanently attached to the PMT assembly in such a way as to illuminate the photocathode of the PMT. The design of this part is not yet fixed but most probably it will be just a cut and polished end of the fibre shining directly on the quartz surface in front of the PMT.

1.4.6 PMT Operation Voltages

All the tests have confirmed that FEU–187 can provide very good time resolution in a wide range of bias voltages and magnetic fields (Figures 1.10 and 1.11). Naturally, increasing HV bias rapidly increases pulse amplitude at the output (by up to 3 orders of magnitude) and changes the relative pulse delay by several nanoseconds. Therefore selection of the optimum HV has a big impact on detector performance and must be made with care. Even a slight change of HV bias necessitates retuning of all delays and thresholds, affecting the efficiency and often also the time resolution.

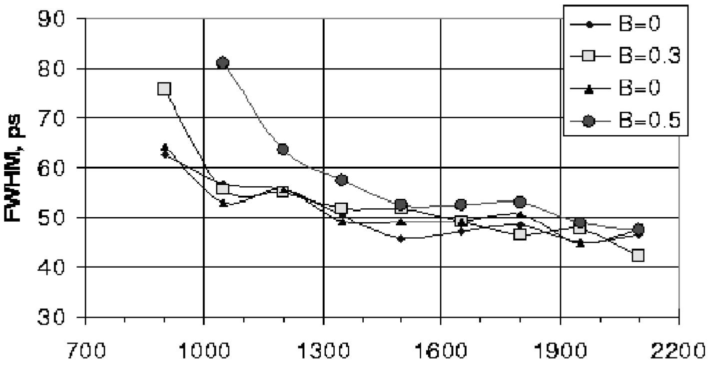

Figure 1.10: Dependency of time resolution on HV bias (V) as a function of external magnetic field strength ($B = 0.3$ and $0.5\,\mathrm{T}$). To demonstrate the consistency of the results two measurements at $B = 0\,\mathrm{T}$ are shown.

Since most of the events in pp and Pb–Pb collisions will be minimum bias events, it makes sense to operate in both types of runs at the same PMT HV. Running at the same voltage is also beneficial for normalization of the results.

While 1 MIP performance is very important, the most interesting heavy–ion events are expected to produce up to 100 MIP signals. This is the main reason why we need signal processing with a sufficiently wide dynamic range to handle all the cases between 1 and 100 MIP. A PMT can produce a maximum signal amplitude of about 5 V. Assuming the linear characteristic of a PMT and taking 5 V for a 100 MIPs signal one obtains the average amplitude of 50 mV for a 1 MIP signal. Due to statistics the amplitude distribution for a 1 MIP particle is very broad, so to get a reasonable efficiency the electronics threshold has to be set at about 1/3 of the average amplitude, i.e. at about 15 mV. These values (15 mV and 5 V) translate to 1:333 dynamic range. Adding a small safety margin the required dynamic range for pulse processing is therefore 1:500. We have shown that it is possible to cope with such dynamic range with a single CFD unit but as a further precaution we shall also amplify the PMT pulses with two different amplification coefficients (1 and 20).

The next important consequence of the 1–100 MIP range is the need to use relatively low HV bias values (about 1000 V) to avoid the distortion of large pulses. We have tested to ensure that even at such low voltages the time resolution remains quite good at 1 MIP and improves with the increase of the light emitted. Keeping the HV bias low we did not encounter pulse saturation up to the 100 MIP level.

To guarantee longevity of the PMT the average anode current (not to be confused with HV divider, which current is larger by nearly 3 orders of magnitude) should be kept below1 μA even if short bursts of

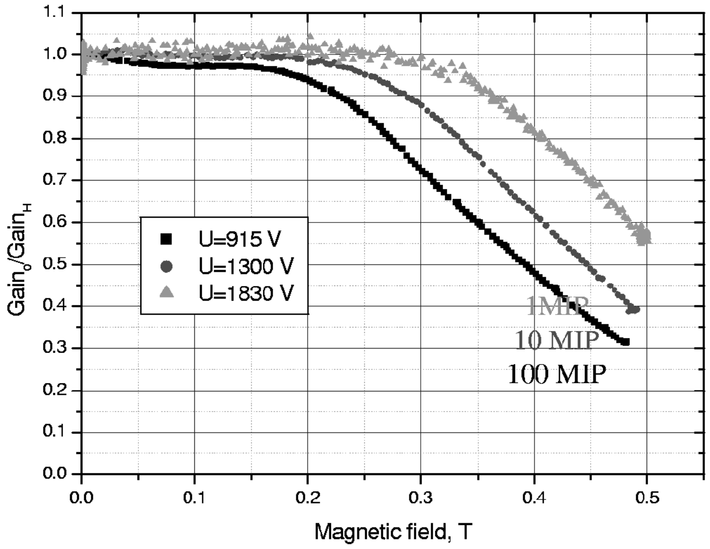

Figure 1.11: Relative PMT gain loss in the magnetic field. HV bias values were set in such a way that the amplitudes of the output signals remained constant for 1, 10, and 100 MIP.

up to 10 μA are acceptable. According to our estimates this condition will be fulfilled with the proposed operation voltage giving 50 mV pulses for 1 MIP. In the calculations we have used nominal luminosities with occupancies and multiplicities generated by PYTHIA and HIJING. If ageing nevertheless takes place it is known from the manufacturer that it will lead to a slow decrease of the gain. This effect is relatively easy to compensate for by increasing the operating voltage. It is also known that after turning HV off for a longer period the PMT partially recovers; its gain factor slowly comes back.

1.4.7 Mechanical Support

A 1:1 mechanical model of T0-C has been build, tested and fully integrated into the central and forward detectors mock–up. The entire support structure (see Fig. 1.12) is made of aluminium. It will be fixed to the muon absorber prior to the installation of V0 and FMD. All the services will be supplied via the dedicated duct (Fig. 1.14) placed on the 12–hour position of the absorber (Fig. 1.13). This location was chosen to minimize the cable length to the TRD "wake-up" box.

1.5 Gain and Time Properties of Fine–Mesh PMTs

The initial studies of the timing properties of fine–mesh phototubes as well as their behaviour in the magnetic field were undertaken in collaboration with Rice University group (USA) and PNPI group (St. Petersburg) for the STAR TOF system [7, 8]. The PMTs under study were Hamamatsu models R5505, and R3432–01, and the Russian FEU–527 produced by the Moscow *MELZ* enterprise in cooperation with the St. Petersburg *Electron* enterprise. Later *Electron* started to produce the same PMTs under the name FEU–187. In 2002 the measurements were repeated at PNPI by the MEPHI group for the latest samples: Hamamatsu R5506 (2 pieces), R3432–01(1 piece) and FEU–187 (similar to FEU–527; 8 pieces). In these measurements light emitting diode was used to imitate a scintillation pulse. We studied the gain behavior at different HV values resulting in a wide dynamic range of the output signals. Typical results of these measurements for FEU–187 are given in Fig. 1.15.

The behavior of the gain in a magnetic field at nominal values of HV does not differ from those obtained for R5505 and FEU–527. At lower voltages the gain falls somewhat faster with the increase of magnetic field compared with nominal high voltage. For all samples we measured the gain in the

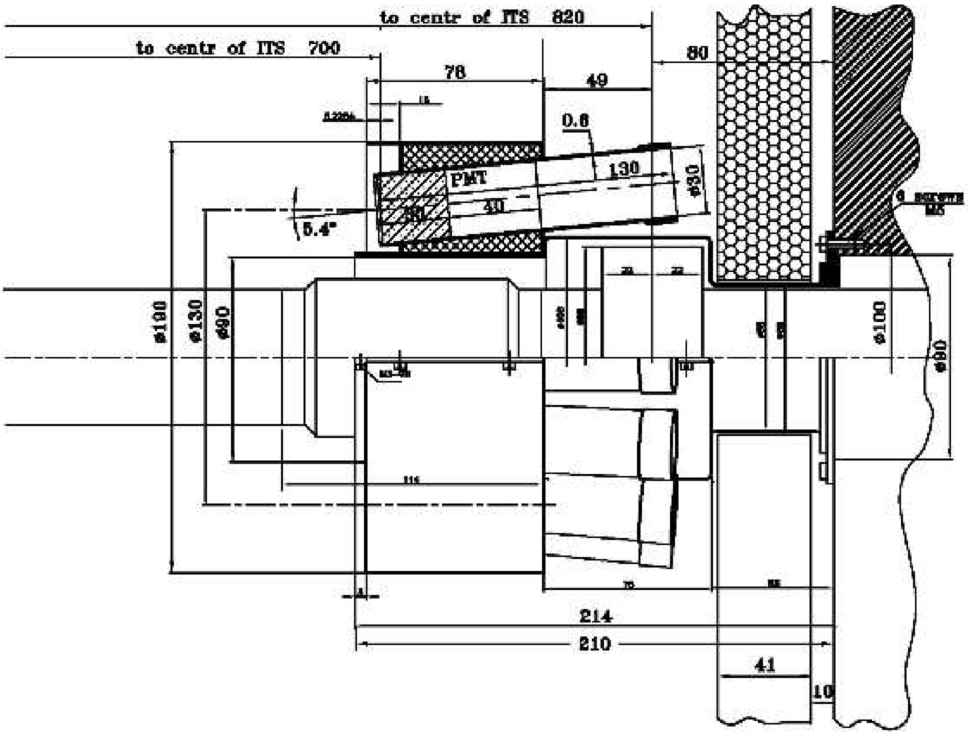

Figure 1.12: Layout of the T0 support on the muon absorber side.

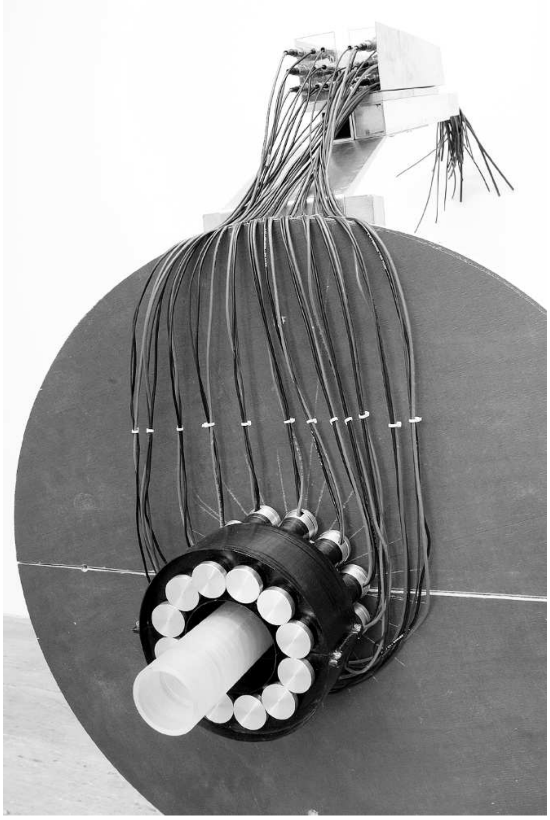

Figure 1.13: Integration test. The plywood structure mocks the muon absorber and the tube, the beam pipe. All cables are fed to patchpanels located in the 12 o'clock duct.

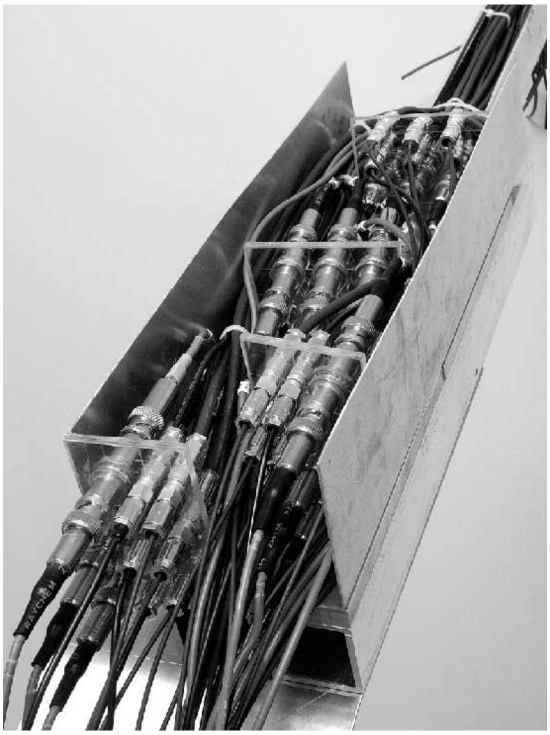

Figure 1.14: T0 patch panels inside the duct on the top of the muon absorber.

magnetic field at voltages corresponding to 100, 10 and 1 % of the nominal gain. Our conclusions are as follows:

1. The differences between the samples are not large.
2. The gain difference for different samples can be easily compensated by changing HV bias.
3. All studied PMTs could operate in magnetic field in a wide dynamic range (1:100).

In order to measure the time characteristics of the tested PMTs at conditions close to those in the Cherenkov detector we have used a pulsed laser (70 ps FWHM). Two types of measurement were made with the laser. In the first run we changed the intensity of the laser pulse and monitored the time resolution and the amplitude. The results are shown in Fig. 1.16.

As expected, the time resolution initially improves with the increase of the light flux and then levels off. At the fluxes expected from the Cherenkov radiator the resolution should stay below 50 ps. Also the flux–amplitude characteristic is good.

In the second run the number of photoelectrons was fixed at about 120–140 and the time resolution and the amplitude were measured as a function of the applied HV. The results of this run are given in Fig. 1.17.

One can see that the time resolution of the fine–mesh PMT FEU–187 remains below 40 ps in a broad dynamic range (at least 1:120) of the output amplitudes. A small decrease in the time resolution at low amplitudes is caused by the increase in electronic jitter [9].

1.5.1 Routine PMT Tests in Magnetic Field

Good test results with selected PMT units cannot guarantee the proper behaviour of the entire production batch. To be sure of that each PMT has to be thoroughly tested in magnetic field. Since each PMT is slightly different, the full set of performance curves at various field and HV settings will be taken

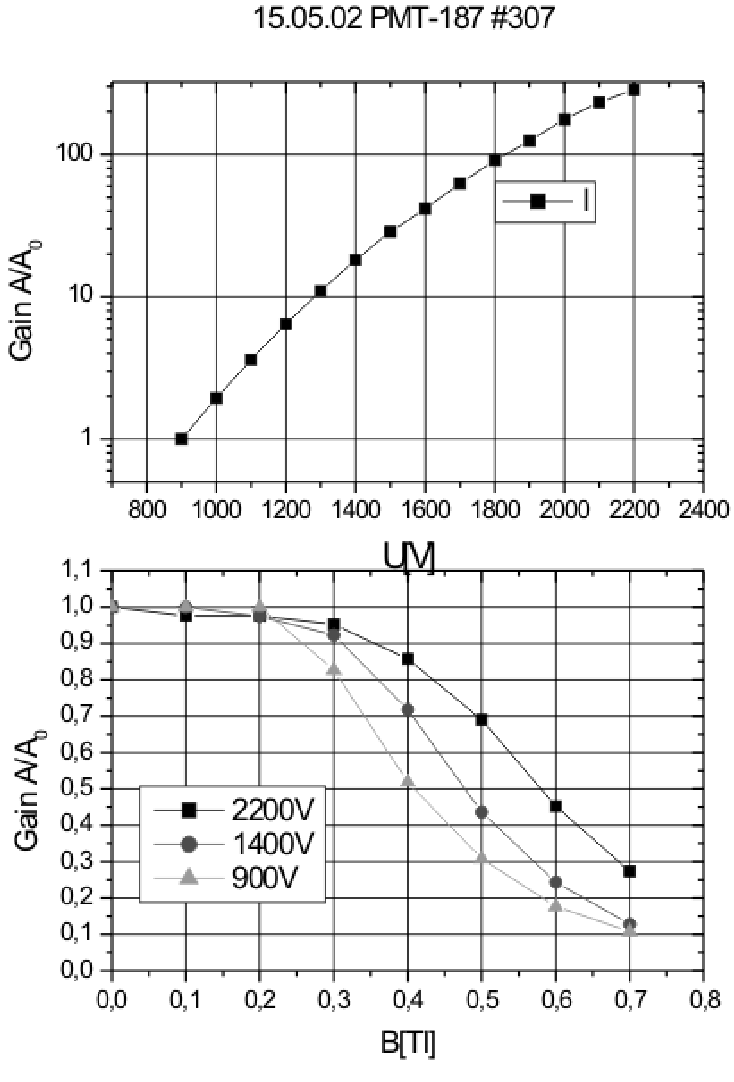

Figure 1.15: Typical characteristics of FEU–187: gain versus high voltage (at 0.5 T magnetic field) and relative gain versus magnetic field at different high voltages.

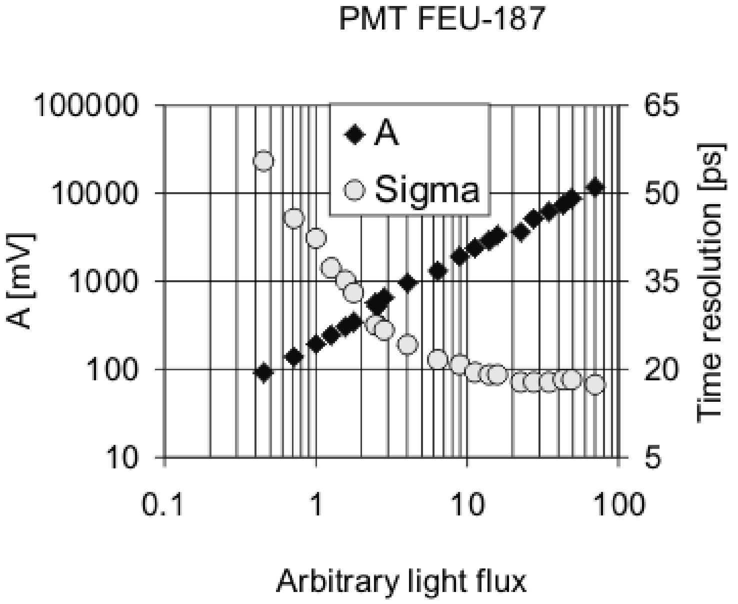

Figure 1.16: Gain and time resolution versus high voltage for typical FEU–187. Arbitrary light flux equal to unity corresponds to approximately 100 photoelectrons.

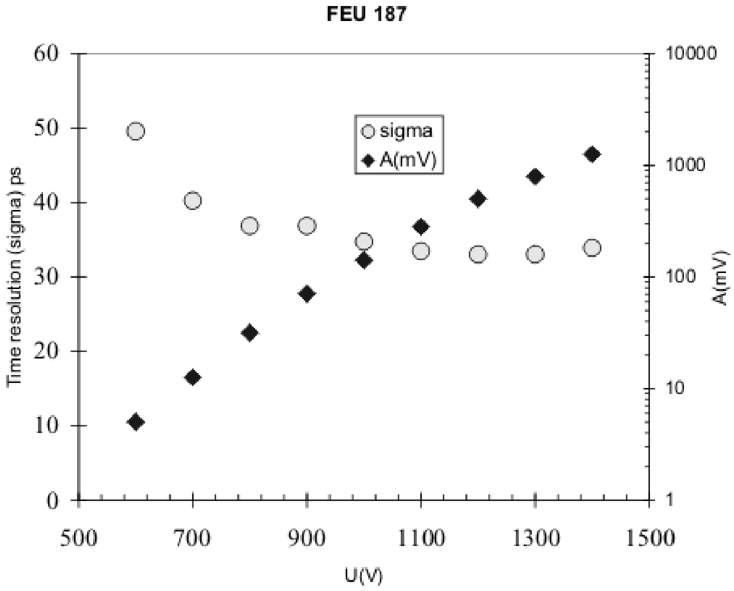

Figure 1.17: Time resolution and amplitudes of the output signal of PMT FEU–187 as functions of high voltage at a fixed light flux equal approximately to 120–140 photoelectrons (1 MIP).

and stored in the detector database. To do that a small air-cooled magnet was designed and constructed (Fig. 1.18). It provides uniform magnetic field of up to 0.5 T inside a volume large enough to accommodate one T0 detector unit. PMT tests with this magnet will be periodically repeated to monitor the performance stability of the T0 modules.

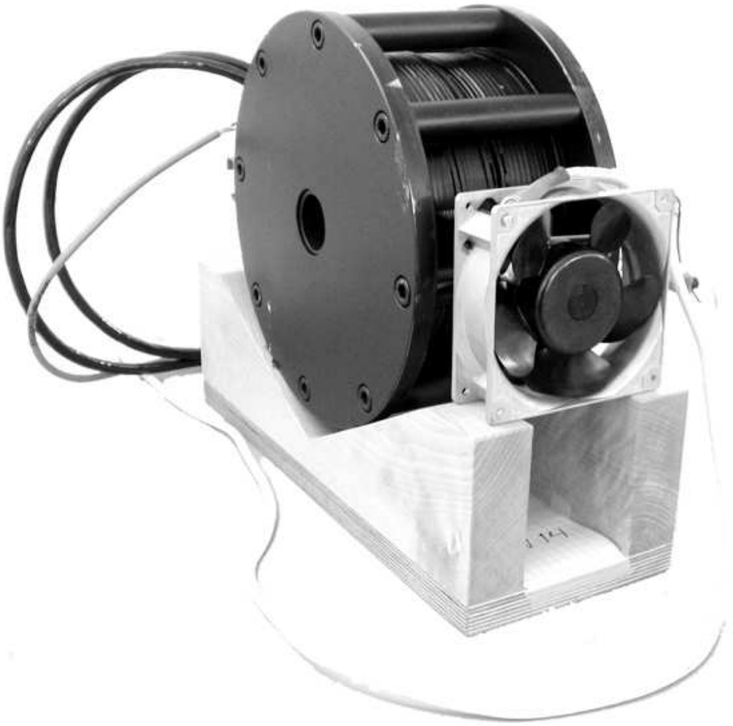

Figure 1.18: A small, air-cooled magnet for testing PM tubes in up to 0.5 T magnetic field.

1.6 Initial Beam Tests of Detector Prototypes

In our R&D studies we have tested different Cherenkov counter option, varying the types of PMTs and radiators. Scintillation counters based on the BC–408 scintillator have also been tested [9–11].

1.6.1 Experimental Setup

For the first tests we used the mixed ITEP pion/proton beam and the experimental setup of the ALICE ITEP group. This setup was also used in the ITEP studies of the timing properties of RPCs for the ALICE TOF detector. The schematic diagram of the test beam setup is shown in Fig. 1.19.

The test beam facility includes several detectors. S1 and S2 are two identical scintillation counters working as START. Each consists of a PMT XP7229 and BC 408 scintillator $2 \times 2 \times 2.5$ cm. The S3 scintillator, located at a flight distance of 10 m from the START, allows the separation of pions from protons ($p = 1.28\,\mathrm{GeV/c}$) with nearly 100% efficiency. Scintillators F1 and F2 form a cross, defining the beam profile to 0.8×0.8 cm. There were also additional scintillation counters S4 and L1 intended for coincidence operation with other counters if needed. The time resolution of each counter was typically about 50 ps. It was continuously monitored during the run.

The investigated Cherenkov detector (CHD) was about 2 m downstream from S1. The signals from S1, and S2 were fed to a constant fraction discriminator inputs, whereas the signals from CHD were fed to a fast leading edge discriminator with a 60 mV threshold. All TDC channels had an identical 50 ps/channel resolution. A 1024 channel QDC was used to measure the amplitude distributions of the CHD signals. All measurements were made at 1.28 GeV/c for both pions and protons.

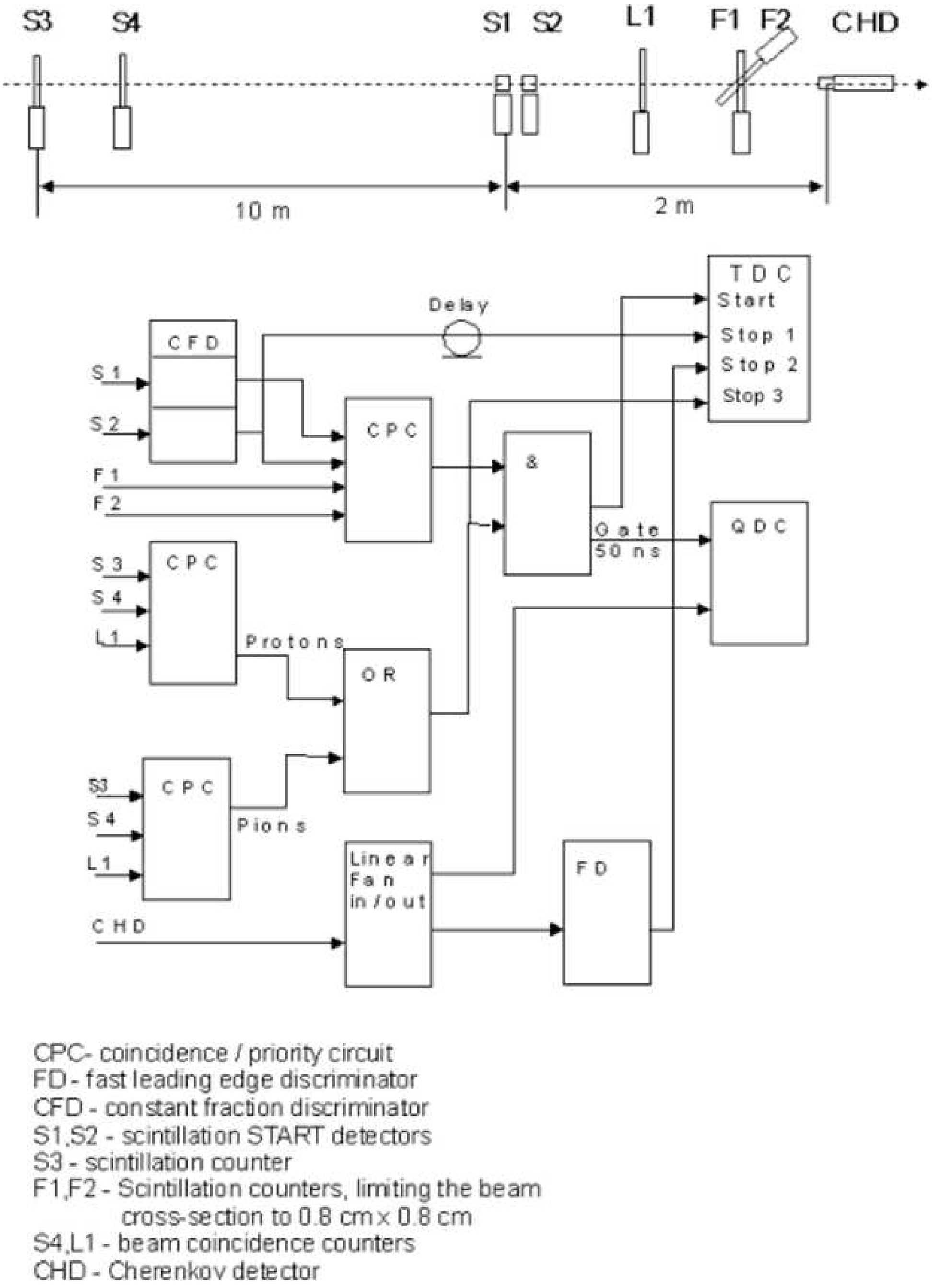

Figure 1.19: Test beam layout.

1.6.2 Experimental Results

We have compared the time resolution of scintillation and Cherenkov detectors using different radiator types and shapes. The scintillation detector used the same PMT but used BC–408 in place of a Cherenkov radiator. The studied radiators included:

1. A cylindrical quartz radiator 26 mm in diameter and 30 mm long.
2. A similar quartz radiator but with a thin Al cover to provide mirror reflection with 98 % efficiency.
3. A Lucite (Plexiglas) radiator of rectangular shape $18 \times 18 \times 30\,\mathrm{mm}^3$.

Among the studied PMTs were Hamamatsu R3432–01 (26 mm diameter) and a Russian fine–mesh PMT FEU–187 (30 mm in diameter). We also used a 20 mm thick BC–408 scintillator with a diameter matching that of the PMT (26 mm and 30 mm correspondingly). A fast leading edge discriminator was used in all runs, and we applied an off–line correction in order to obtain the final time resolution values of each different type of detector.

All our measurements were made at two geometries of the beam: a limited rectangular cross–section beam $0.8 \times 0.8\,\mathrm{cm}^2$ defined by the F1 and F2 counters, and a broad beam illuminating the whole detector. The amplitude distributions of the PMT output signals differed significantly for these two geometries. In the first case all radiator types produced a single–peak Gaussian distribution. In the second case the amplitude distribution consisted of two peaks (Fig. 1.20).

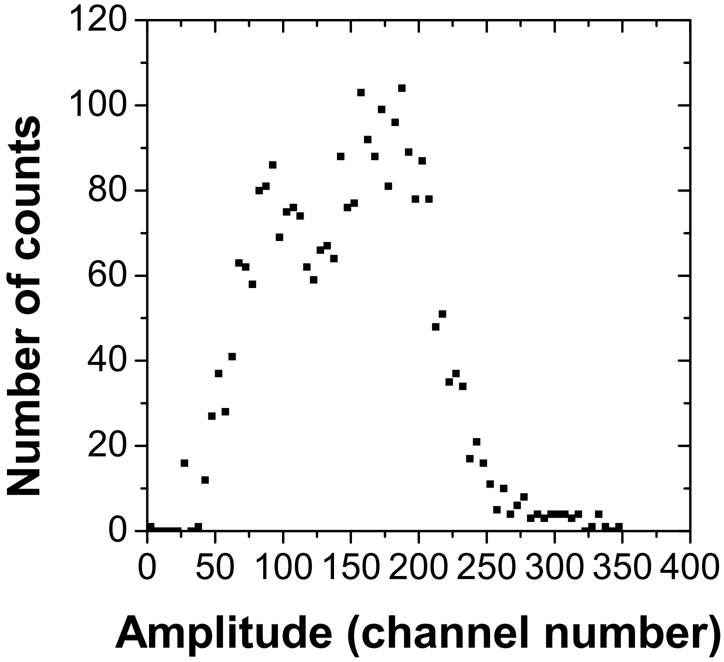

Figure 1.20: Amplitude distribution of PMT output signals for “broad” beam geometry for pions 1.28 GeV/c (cylindrical quartz Cherenkov radiator).

The right–hand part (high–amplitude) of the double peak coincides roughly with the position of the single peak registered with the limited beam. The left–hand bump is at half the amplitude value. A similar amplitude distribution for the broad beam geometry was obtained by the Hiroshima group in the PHENIX experiment [6]. Monte Carlo simulations explain this doubling effect quite well, as will be shown in the next section.

A summary of our results is collected in Table 1.3 and Table 1.4. It is clear that Cherenkov counters give better performance than the BC–408 scintillator. As far as time resolution is concerned both Lucite and quartz radiators are acceptable. The advantage of a Lucite radiator is a smaller radiation length. The radiation length of Lucite is $X0 = 34.4\,\mathrm{cm}$, whereas for quartz $X0 = 11.7\,\mathrm{cm}$. A 3 cm quartz radiator makes about $0.25X0$ as compared to $0.1X0$ for 3 cm of Lucite. However, the radiation stability of Lucite is only 100 krad, which is substantially less than the expected cumulative dose for the T0 detector. This was the main reason for choosing quartz radiators.

Table 1.3: Typical time resolution values obtained with different PMTs, radiators and scintillators.

Beam geometry PMT	**Radiator/scintillator**	**Time resolution**
R3432–01	Quartz diam 26 × 30 mm	40 ps
FEU–187	Quartz diam 26 × 30 mm	42 ps
R3432–01	BC–408, diam 26 × 20 mm (with a diffuse reflection)	57 ps
FEU–187	BC–408, diam 30 × 20 mm (with a diffuse reflection)	55 ps
R3432–01	Aluminized quartz diam 26 × 30 mm	48 ps
Broad–beam geometry		
R3432–01	Quartz diam 26 × 30 mm	55 ps
FEU–187	Quartz diam 26 × 30 mm	57 ps
R3432–01	BC–408, diam 26 × 20 mm (with a diffuse reflection)	80 ps
FEU–187	BC–408, diam 30 × 20 mm (with a diffuse reflection)	89 ps
R3432–01	Aluminized quartz diam. 26 × 30 mm	54 ps
R3432–01	Plexiglas radiator 18 × 18 × 30 mm	45 ps

Table 1.4: Results from ITEP accelerator, pions 1.28 GeV/c, March 2, 2002. Broad–beam geometry. Both Lucite and quartz radiators were 30 mm long and their diameter was matched to that of the PMT (26 mm for Hamamatsu and 30 mm for FEU–187)

Run No.	**Type of PMT**	**Type of radiator**	**Time resolution, ps**
3	Hamamatsu R3432–01	Quartz	53
3	Hamamatsu R3432–01	Lucite	50
7	Hamamatsu R3432–01	Lucite	54
8	Hamamatsu R3432–01	Lucite	56
9	Hamamatsu R5506	Quartz	59
10	Hamamatsu R5506	Lucite	75
11	FEU–187	Quartz	55
12	FEU–187	Quartz	58
13	FEU–187	Quartz	52
14	FEU–187	Quartz	42

1.7 Monte Carlo Simulations

Adequate description of the response function of a Cherenkov counter is needed to simulate experimental data and to estimate the influence of the secondaries scattered by surrounding detectors on the performance of the T0 detector. In our first approach we did not use AliROOT because our goal was to compare the results of the simulations with the experimental data obtained in our beam tests. The simulations were based on GEANT 4.2 and confirmed with GEANT 3. We have added own program modules (in C++) describing the conditions of our experiments.

1.7.1 Detector Response Function

We have made simulations of the following beam profiles: narrow, limited ($0.8 \times 0.8\,\mathrm{cm}^2$) beam geometry) and broad beam geometry. In all cases we have assumed fully random, uniform flux of $\beta = 1$ particles flying parallel to the symmetry axis of the Cherenkov counter. The simulations were made for PMT R3432–01 with a quartz radiator 30 mm in diameter, and 30 mm long.

In the narrow beam geometry all particles followed exactly the same path so the light collection efficiency was constant and the PMT output pulse distribution follows the Poisson distribution of photoelectrons emitted from the photocathode. The result of this simulation for particle trajectories on the axis of the counter is shown in Fig. 1.21.

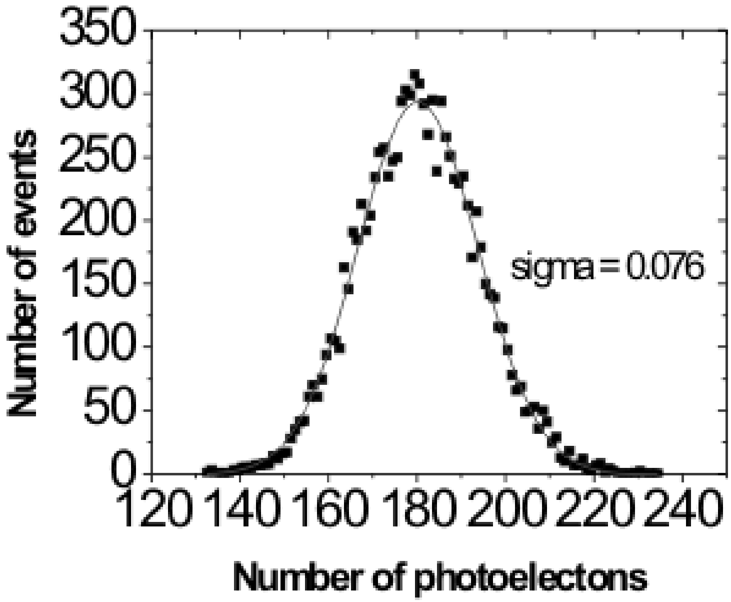

Figure 1.21: Monte Carlo simulations of the number of photoelectrons emitted by particles with $\beta = 1$ traversing the cylindrical quartz Cherenkov radiator along its central axis.

$\langle N \rangle \approx 180$ is the mean number of photoelectrons emitted from the photocathode in response to the Cherenkov light produced in 3 cm of quartz by a relativistic particle. This result is in good agreement with the estimate presented in Section 1.4.3. The value $\eta = 0.15$ was taken as the average of the quantum efficiency of the photocathode in the 300–550 nm wavelength range. The extracted width parameter $\sigma = 0.076$ is consistent with 0.075 calculated placing $\langle N \rangle = 180$ to the formula $\sigma = 1/\sqrt{\langle N \rangle}$.

Since the photocathode of a fine–mesh PMT covers only about 45% of the surface of the entrance window, light collection drops sharply at the edges, as illustrated in Fig. 1.22. This explains the double peak character of the amplitude distribution measured in the broad beam geometry (shown in Fig. 1.20). Figure 1.23 demonstrates the results of Monte Carlo simulations based on the response function of a Cherenkov detector with a cylindrical quartz radiator to the broad beam profile (approximated by realistic two–dimensional Gaussian distribution of the density of the particles in the beam, with $\sigma = 0.85\,\mathrm{cm}$).

In actual ALICE conditions the amplitude distribution of the Cherenkov counters' outputs will be somewhat different from those in Fig. 1.23 because of the changing position of the IP. Gamma rays, originating from the IP and subsequently converting into electron–positron pairs, should also be taken into account. We have done that by implementing into AliROOT subroutines the response function of the Cherenkov counters and generating events with PYTHIA [6.125]. The resulting amplitude distributions for T0-C (0.7 m from the IP, on the muon absorber side) and for T0-A (3.6 m from the vertex on the RB24 side) are given in Fig. 1.24 (without and with the background induced by the beam pipe background).

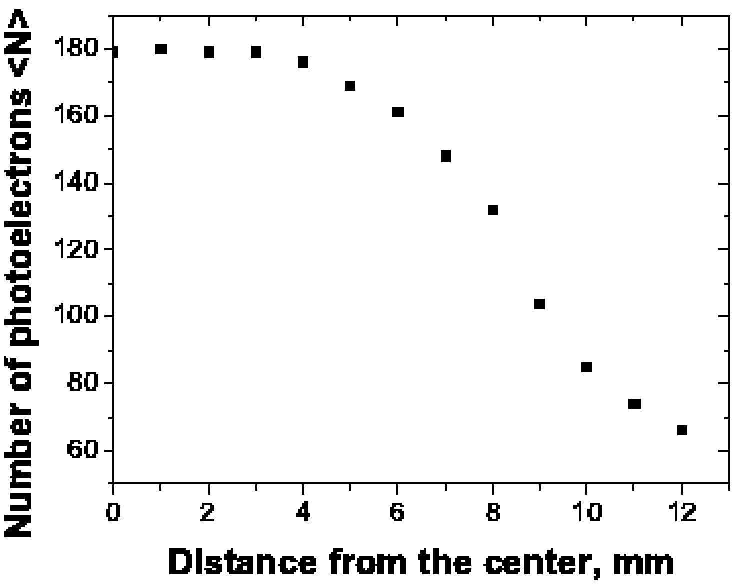

Figure 1.22: Mean number of photoelectrons $\langle N \rangle$ emitted by particles with $\beta = 1$ traversing the cylindrical quartz radiator at different distances from the centre.

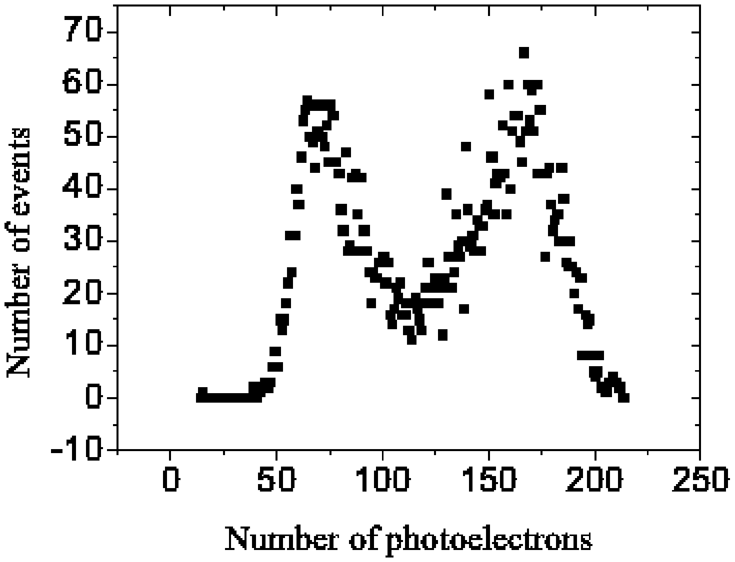

Figure 1.23: Monte Carlo simulations of the number of photoelectrons emitted by particles with $\beta = 1$ in the cylindrical quartz radiator and “broad” beam geometry with “realistic” beam density distribution.

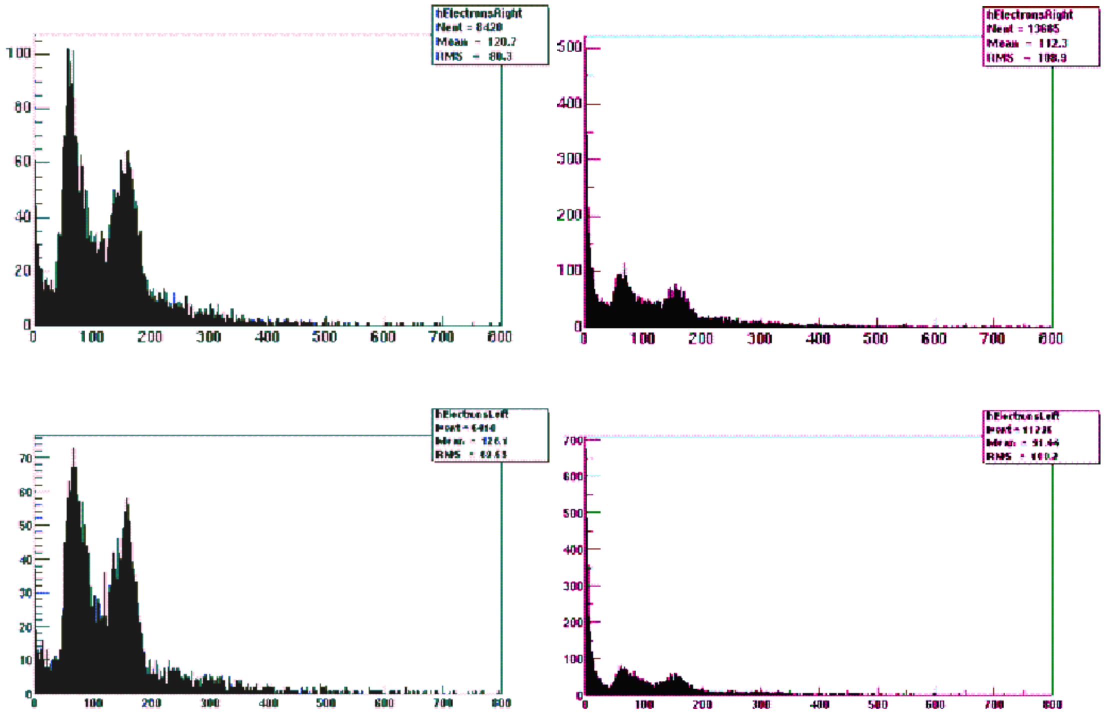

Figure 1.24: Amplitude distributions for the Cherenkov counter in the T0-C (top), and the T0-A (bottom) given by PYTHIA version 6.125. On the left hand side background from the beam pipe is not taken into account, the right hand side does include this background.

1.7.2 T0 Efficiency in pp Collisions

The triggering efficiency of the T0 detector in heavy–ion collisions (due to high multiplicities of produced particles) is nearly 100% and therefore is of no concern at this point. But in pp collisions the involved multiplicities are much smaller and the expected efficiency must be carefully simulated, taking into account not only the response function of the Cherenkov detector but also all the details of geometry, location and thickness of the beam pipe, support structures, etc. In carrying out these simulations we have considered a particle to be registered if the signal from the PMT was larger than 40 photoelectrons. This threshold value was based on our actual experimental data. The background from the interaction of primary particles coming from the IP with the beam pipe was also taken into account. The results of these simulations were shown in Section 1.4.4 (Figures 1.5 and 1.6). Table 1.5 summarizes the calculated efficiencies extracted from the data for all events generated by PYTHIA.

Table 1.5: Calculated efficiencies of the T0 detector for pp collisions

	Right array	**Left array**	**Both arrays in coincidence**
Physical efficiency without beam pipe	62%	58%	43%
Geometrical efficiency without beam pipe	64%	59%	45%
Physical efficiency with beam pipe	67%	60%	48%

The increase of the physical efficiency in the presence of the beam pipe is caused mainly by the conversion of gammas into electrons in the material of the pipe. The efficiencies given in Table 1.5 are averaged over all multiplicities. Efficiency at multiplicities larger than 20 is given in Fig. 1.25.

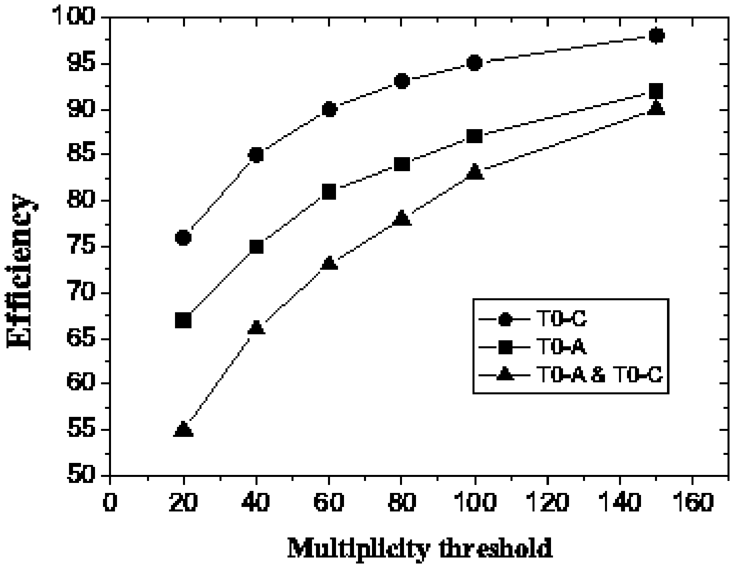

Figure 1.25: Efficiency of registration of pp collisions as function of total multiplicity of events.

At multiplicities $M > 150$ the efficiency of the T0 detector (coincidence of T0-A and T0-C) is already about 90%. It is therefore obvious that for ion–ion collisions the efficiency will be 100%, excepting the ultra–peripheral collisions.

1.7.3 Simulations of Multiplicity Resolution

The T0 detector should generate 3 trigger signals corresponding to the 3 multiplicity levels: minimum–bias, semi–central, and central ion–ion collisions. Such signals could be produced, for instance, by analysing the sum of all PMT pulses with discriminators. Obviously, this procedure will work only in the case of high multiplicities (i.e. for ion–ion collisions). In pp collisions the average occupancy per Cherenkov counter is only about 0.3, making multiplicity determination impossible.

To estimate T0 multiplicity resolution from the sum of PMT signals we have used a simple step–by–step approach. First we estimated multi–particle resolution of a single Cherenkov counter in broad–beam geometry. This can be done in two ways. As the distribution of the particles is random and uniform across the surface of the radiator, one can simply sum the number of photoelectrons for 2 particles, 3 particles, etc. Typical results for this procedure are given in Fig. 1.26. When the number of particles exceeds 3 the photoelectron distribution becomes Gaussian.

The other way is to calculate directly the dispersion $D = \langle n^2 \rangle - \langle n \rangle^2$. For the distribution given in Fig. 1.23 $D = 1936, \sigma_0 = D^{1/2} = 44$ (r.m.s.) and the relative error is $\delta_0 = \sigma_0 / \langle N \rangle = 0.39$ ($\langle N \rangle = 112$). For n particles $\delta_n = \delta_0 / \sqrt{n}$. The results of these calculations are given in Fig. 1.27.

The dashed curve is the function δ_n. The rhombs give the values of deltas obtained from the Gaussian fits of the distributions similar to Fig. 1.26. The solid curve represents the Poisson fluctuations of the number of particles' relative statistical error $\delta = 1/\sqrt{n}$. It is clear that the resolution of a Cherenkov counter for multi–particle events is approximately two times better than the statistical error.

Figure 1.24 characterises the Cherenkov counters' response to the random flux of relativistic particles parallel to the counter axis. Under actual ALICE conditions the angular distribution of particles, gamma ray conversion in the radiator, and the background induced by the beam pipe should also be taken into account. Since full treatment requires a lot of computer time we have settled for simplified approach. To simulate multi–particle resolution of the detector we have used a parametrized HIJING event generator. The multiplicity of events was fixed at a certain value, corresponding to the average number of primary charged particles per Cherenkov counter equal to unity. In the course of simulations (10 000 events)

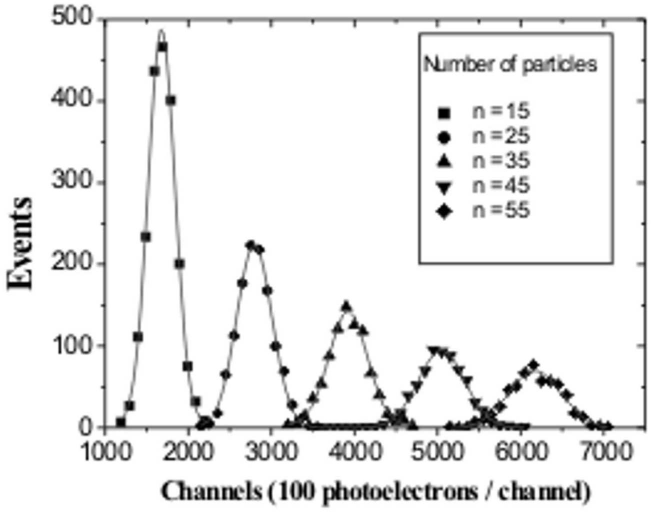

Figure 1.26: Monte Carlo simulations of response functions of a Cherenkov counter for *n* particles randomly distributed across the surface of the radiator.

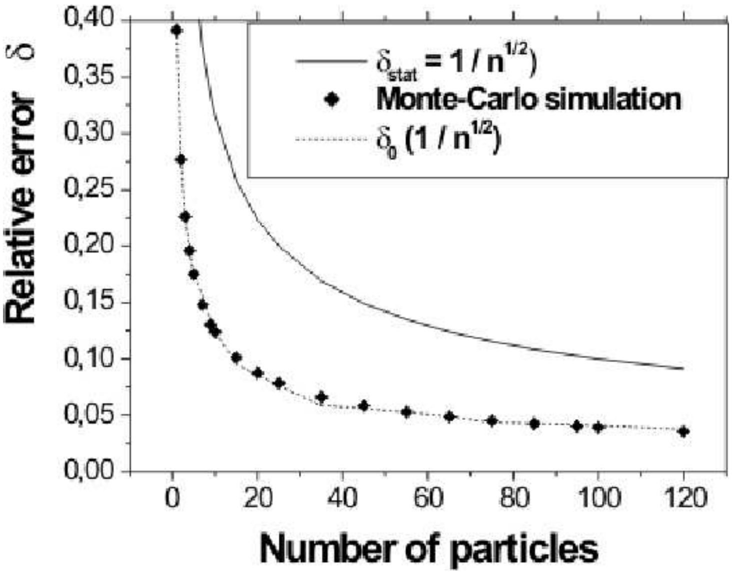

Figure 1.27: Relative statistical errors for the registration of multi–particle events for parallel random charged particles' flux.

we have fixed each amplitude in each Cherenkov counter for each event. The primary gamma–ray conversion in the radiator, as well as the secondary particles (electron–positron pairs and δ-electrons), were also taken into account. The resulting amplitude distribution, averaged over all counters and events, in a single Cherenkov counter is shown in Fig. 1.28. The relative error δ_0 of this distribution is equal to 1.04 (compared to the value 0.39 obtained for the narrow beam geometry hitting the center of the radiator).

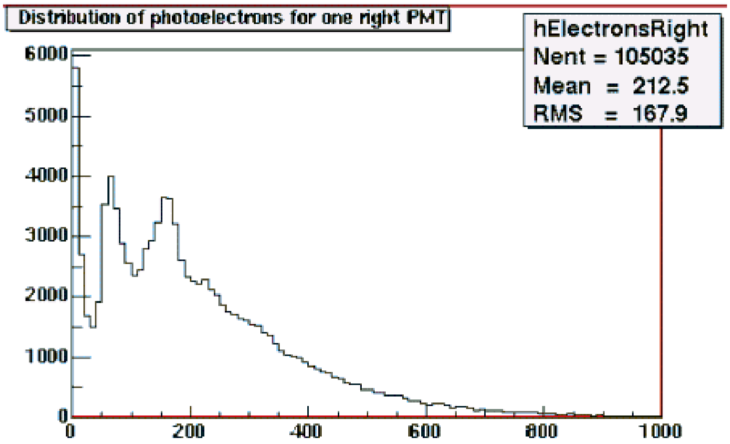

Figure 1.28: Amplitude distribution in one PMT from the (T0-C), averaged over 10 000 HIJING events. Zero amplitudes are excluded from the distribution for reasons of scaling.

The sum of the signals coming from the 12 PMTs of the T0-C and averaged over all events is shown in Fig. 1.29. The shape of this amplitude distribution approaches Gaussian distribution. The relative error δ_0 of the distribution is equal to 0.295, practically equal to that of the distribution for a single PMT divided by $\sqrt{12}$.

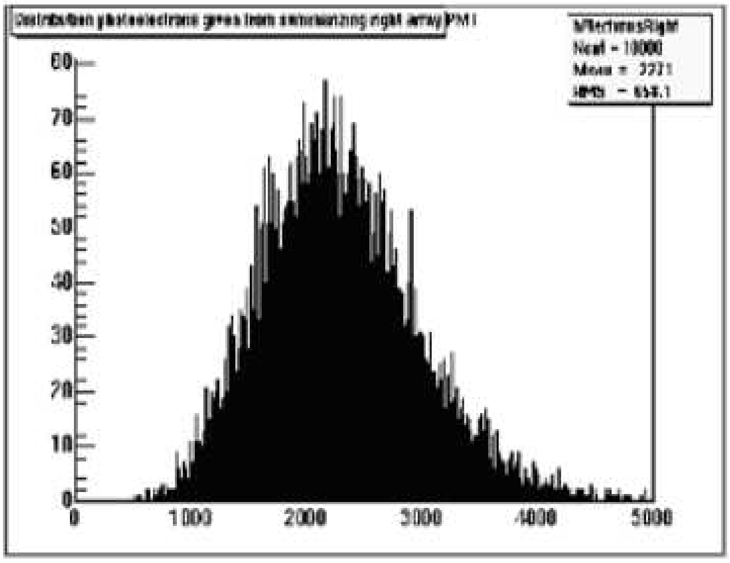

Figure 1.29: Averaged over 10 000 HIJING events, the amplitude distribution of the sum of 12 PMTs' amplitudes in the T0-C.

Note The distributions given in Figures 1.28 and 1.29 include the statistical Poisson distribution of the primaries coming from IP. This Poisson distribution for primary charged particles registered in the T0-C is shown in Fig. 1.30.

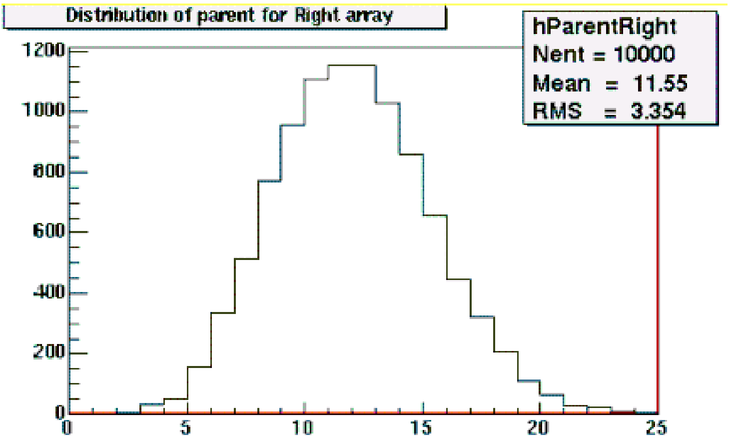

Figure 1.30: Poisson distribution of the number of primary charged particles registered by the T0-C in one HIJING event at fixed multiplicity, corresponding to 1 primary charged particle per Cherenkov counter.

The multi–particle resolution of the array when the average number of primary charged particles per Cherenkov detector is equal to 2, 3, and 4 was obtained by summing the amplitudes for 2, 3 and 4 events.

It is interesting to compare these results with the case when only statistical Poisson fluctuations of the number of primary charged particles are taken into account. Figure 1.31 shows the statistical Poisson fluctuations as a function of the mean number of particles (solid line).

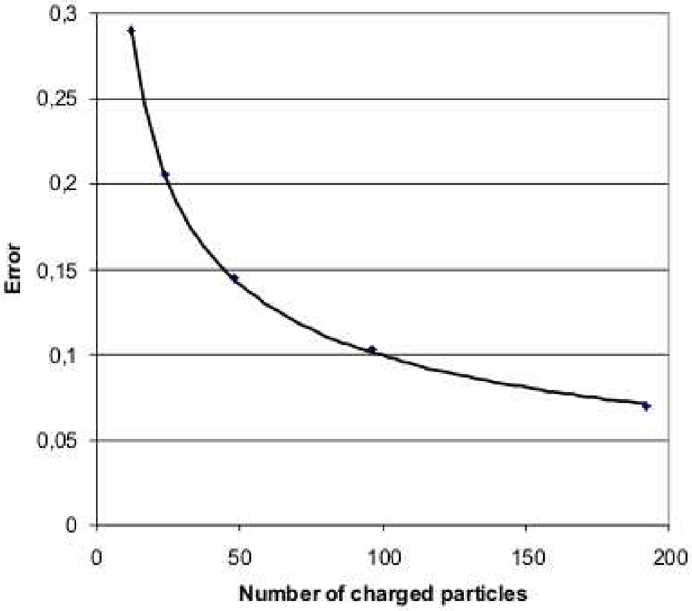

Figure 1.31: Relative statistical errors for the registration of the number of primary charged particles by the T0-A. Solid line – Poisson statistics, rhombs – detector resolution obtained by Monte Carlo simulations.

The rhombs show the statistical errors of charged particle multiplicities defined as above. This coincidence may be explained by taking into account that every Cherenkov counter registers not only primary charged particles but also some primary gammas (which contribute about 20 % of the signals) and charged particles from the beam pipe, the number of which is correlated with the primary statistics. The results of the simulations show, that the actual number of charged and neutral particles registered by each counter is two times larger than the number of primary charged particles. The same simulations were carried out for the T0-A at a fixed multiplicity corresponding to the mean number of primary charged particles per single Cherenkov counter in the array and being equal to one. The results of the simulations practically coincide with those given in Fig. 1.30 for T0-C.

In conclusion one can say that the multi–particle resolution for primary charged particles of both arrays is determined almost solely by Poisson statistics (statistical error).

1.8 Fast Electronics

The overall diagram of T0 electronics is shown in Fig. 1.32. Signals from each PMT are first sent to the so-called shoeboxes, located about 6 m from the detectors. The main role of the shoeboxes is to split and amplify the signals to generate a wake–up call for the TRD detector. Otherwise no electronics would be required between the PMTs and the main electronics racks of T0 outside the L3 magnet. There the T0 pulses are processed and used to produce the required trigger signals. The time and amplitude information from each PMT will be read out and stored by ALICE DAQ. The T0 readout will be nearly identical to that of the TOF detector. This solution was adopted to cut costs and to guarantee the performance of the T0. Currently TOF is the only ALICE sub-detector that needs non-trigger information from T0.

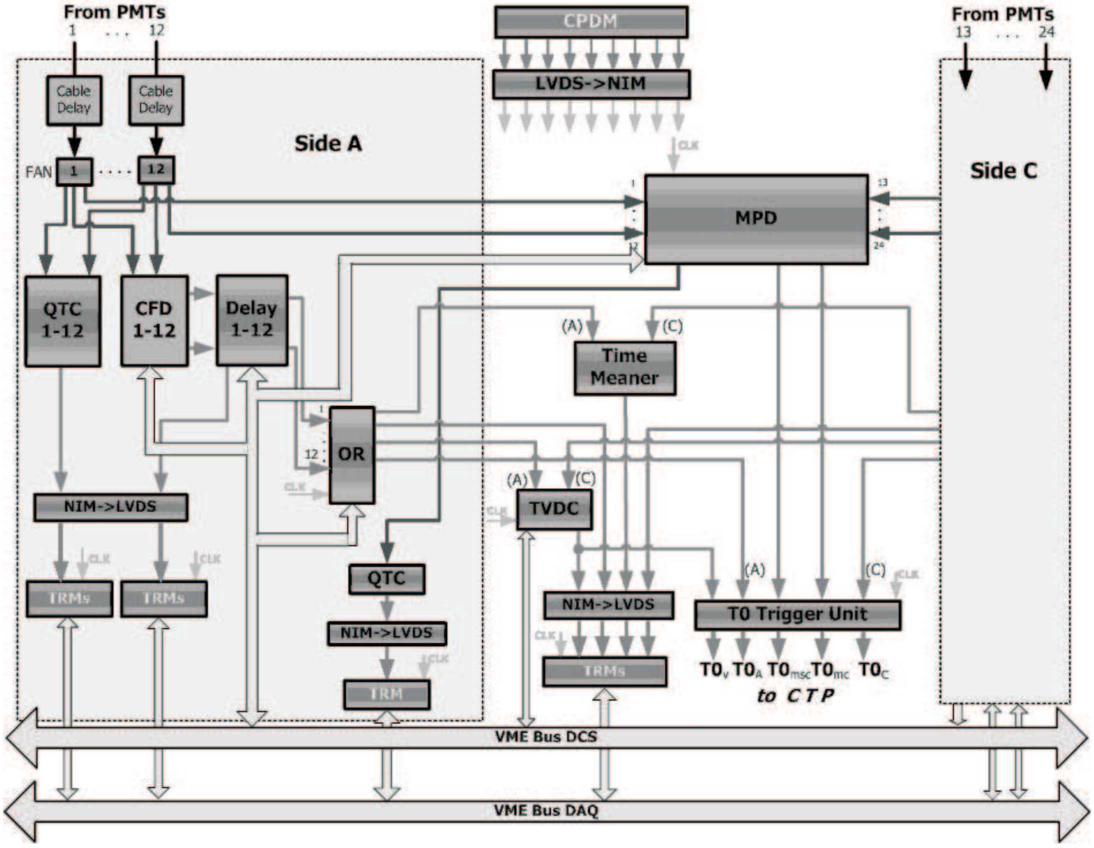

Figure 1.32: T0 fast electronics.

1.8.1 Shoebox with front–end electronics

There will be two separate shoeboxes, one for each arm of the T0 detector. The T0-A shoebox will be a stand-alone unit containing only the electronics for splitting and amplifying the signals. The T0-C shoebox will be in direct proximity to the TRD wake–up shoebox, where the pulses from all T0 and V0 detector will merge and be processed in a similar fashion.

As discussed in Section 1.4.6 the expected signal amplitude of the input to the shoebox will be from 15 mV up to 5 V. To secure 50 ps time resolution throughout the entire dynamic range it is necessary to preserve as much of the signal's original shape as possible. To prevent the zero level from floating with changing count rate, the ultra–wideband amplifier in the shoebox should be of the direct current type.

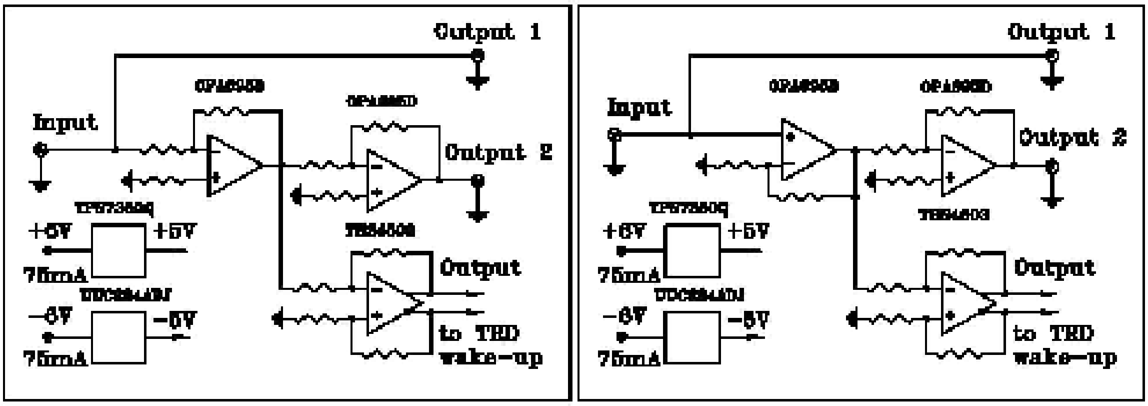

Figure 1.33: Block diagrams of the amplification stage of the shoebox as tested at CERN, 2004 (left), and the improved version (right).

Figure 1.33 shows the "shoebox" used during the June 2004 run and the modified design that will be tried out next. Each channel of the shoebox has one input for PMT pulses and 3 outputs: 1 direct and 2 with gain of about 25. The direct output will go to the wide range CFD (see the next section). In principle, if the CFD works as expected in the full dynamic range, the amplified signal will only be used to improve the accuracy of amplitude digitization. In case of unforeseen problems, the amplified output could also feed to the second CFD working in parallel with the one with the direct signal, allowing for precise off-line corrections.

The TRD wake–up electronics does not need the same time resolution as TOF. Since small time shifts such as those due to saturated pulses are not a problem for the wake–up, and the absence of low amplitude (not amplified) pulses makes the design easier and more tolerant of electronic noise and interference, only the amplified signals will be delivered to the TRD wake–up electronics.

The main construction elements of the shoebox are the OPA695 current-feedback operational amplifier and THS4503 - a wideband, low-distortion fully differential amplifier. Since even these modern operational amplifiers provide the proper bandwidth only for gain below 8, we have had to use a two-stage system, each with gain of about 5. The Printed Circuit Board (PCB) of the prototype was 80 mm × 75 mm and included two low-dropout voltage regulators providing the amplifier with a clean and stabilised power supply. In the quiescent mode the unit consumes 75 mA from +6 V and from -6 V. At high counting rate the current will increase to 100 mA.

For the next version of the prototype the size of the PCB will be reduced to $50 \times 60\,\text{mm}^2$ and a non-inverting stage will be used to eliminate the passive fan out at the input, which currently gives a slight (50/70) attenuation.

1.8.2 Constant Fraction Discriminator with Wide Dynamic Range

Constant Fraction Discriminators (CFD) are used to determine the arrival time of analogue pulses from fast detectors. As long as the amplitude of the pulse stays within the dynamic range of the CFD, no slewing corrections are needed. The time does not depend on the amplitude of the pulse. A very good CFD, for instance the Phillips Scientific 715 [13] exhibits typical time walk plus slewing of ±75 ps for amplitudes between threshold and 100 times threshold. As discussed in Section 1.4.6, the dynamic range required in ALICE experiments will be 5 times larger. In principle, off-line slewing corrections are a standard procedure that enables good time resolution even with simpler Leading Edge discriminators (LED). However, considering the need for good on-line performance (trigger) and to stay below the 50 ps range in time resolution, we opted to develop a CFD that will work in a dynamic range of 1:500 (see Fig. 1.34).

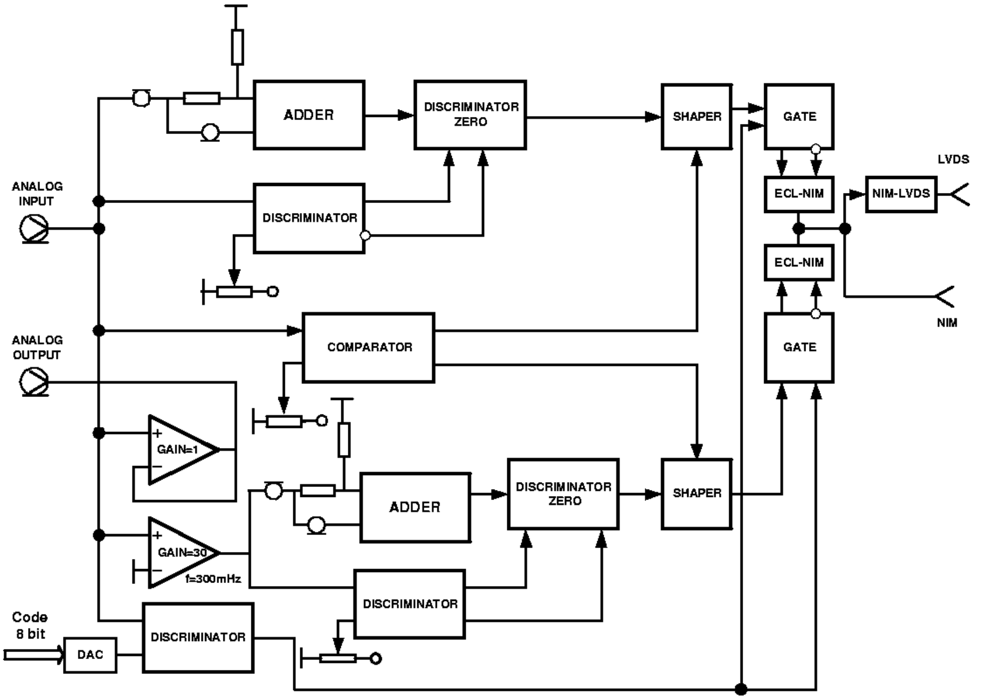

Figure 1.34: Schematic diagram of the prototype of the wide range CFD.

The timing channel of the CFD is implemented according to the traditional scheme, with the detection of zero crossing using an inverted, delayed and attenuated signal. The main difference is in the use of the two signals (amplified and without amplification) instead of just one. In this way our CFD is in fact two CFDs working in parallel and governed by a comparator of output signals. The delay and attenuation values are set by input signal parameters. A lot of attention was paid to the design of the wide-range amplifier. It provides relatively high amplification ($K_{amp} = 22$) while retaining the characteristics of the original input signal. The use of the amplifier is crucial for extracting time signals with low amplitude. On the tested prototype the lowest discrimination level was 4 mV and was restricted only by the noise level of the amplifier stage. The threshold level is set using 8-bit code. The utilization of two channels makes it possible to obtain a timing accuracy of $T = \pm 25$ ps while the input signal ranges from 4 mV to 3 V. The amplitude discriminator commutates the output signals from the first or second timing channels depending on the amplitude of the input signal. The output shapers of the unit generate the signals in NIM and LVDS standards, matching the requirements of the receiving units.

The buffer amplifier incorporated into the tested CFD prototype has gain $K = 1$ and serves as an input signal splitter.

1.8.3 T0 Vertex Unit

Determination of the IP of each collision and comparing it to preset minimum and maximum values is one of the main trigger functions of the T0 detector. The unit intended to perform these operations is the T0 Vertex Unit or TVDC. The main parameters of the TVDC are determined by the expected size of the interaction area (0.7 m), nominal resolution of the measurements (±1.5 cm), and the working frequency of the LHC (40 MHz). Accordingly, the TVDC should meet the following requirements:

- time range of ±2.5 ns(5 ns);
- nominal time resolution of 20 ps (for 8-bit conversion);
- total dead time below 25 ns.

The block diagram of the tested prototype is shown in Fig. 1.35.

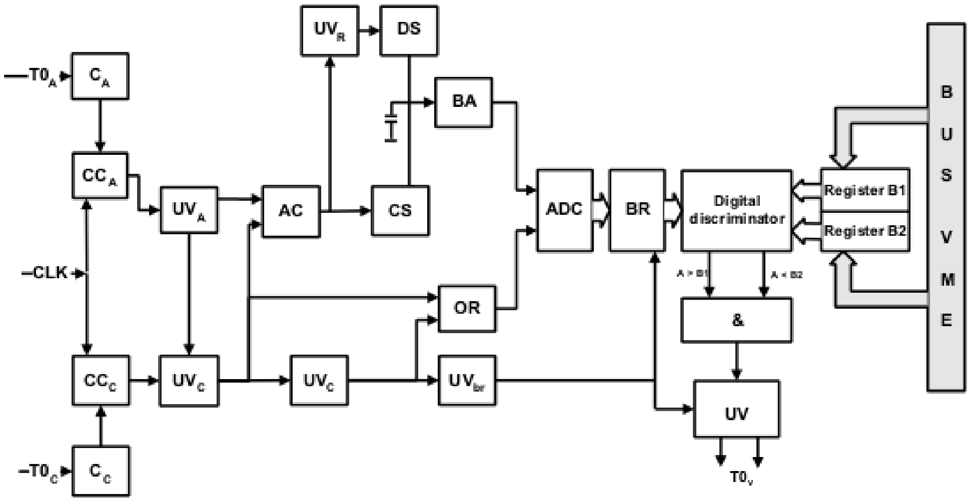

Figure 1.35: TVDC unit.

C = Comparator
CC = Coincidence Circuit
UV = Univibrator
AC = Anticoincidence Circuit
CS = Charging current Switch
DS = Discharge Switch
BR = Buffer Register
ADC = Amplitude-Digital Converter
BA = Buffer Amplifier
& = AND circuit
OR = OR circuit.

The main components of TVDC are the Time to Amplitude Converter (TAC) followed by a flash ADC with digital discriminators for T0 Vertex signal generation. The TAC is designed to generate an output signal only when both input signals come within the allowed time interval (4 ns) and in the presence of the LHC clock signal (or Bunch Crossing signal). The 8–bit flash ADC AD9002 used in the prototype has the encoding frequency 150 MSPS, and 20 ps granularity. The digital comparator K1500CP166 has a delay equal to 3 ns. It generates the T0 Vertex output signal when the code of the flash ADC coincides with one of the preset (allowed) codes of the vertex position. The total dead time of the TVDC unit is, as expected, below 25 ns.

The performance of the first prototype of the T0 Vertex Unit obtained during the July 2003 test run at CERN is shown in Fig. 1.36.

1.8.4 T0 Multiplicity Discriminator

The Multiplicity Discriminator (MPD) generates three logical signals corresponding to the three pre-set levels of desired particle multiplicity. The MPD output goes to Trigger Signal Module (TSM) where all the other T0 trigger signals are converted to the form acceptable by the Central Trigger Processor (CTP). In addition to the trigger function MPD generates analogue sum that will be digitized and stored by ALICE DAQ. The block diagram of the first prototype to be successfully tested at CERN (in June 2004) is shown in Fig. 1.37.

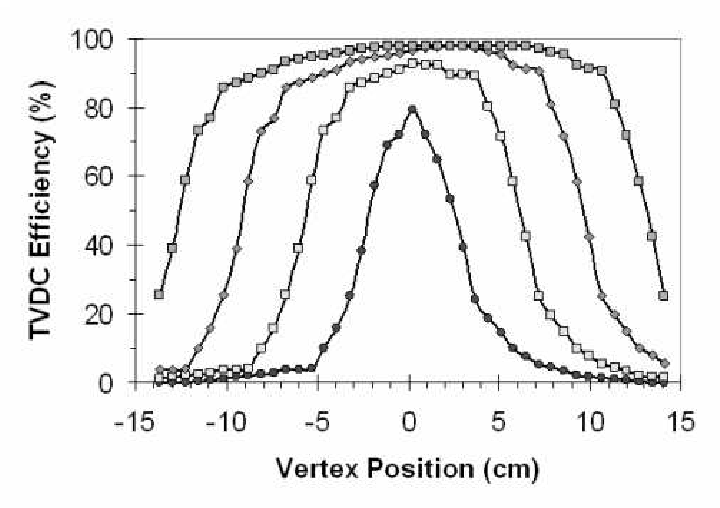

Figure 1.36: Performance of the first prototype T0 Vertex Unit during the July 2003 test experiment using PS beams at CERN. The four curves illustrate trigger efficiency as a function of vertex position recalculated for 4 different settings of the upper and lower threshold.

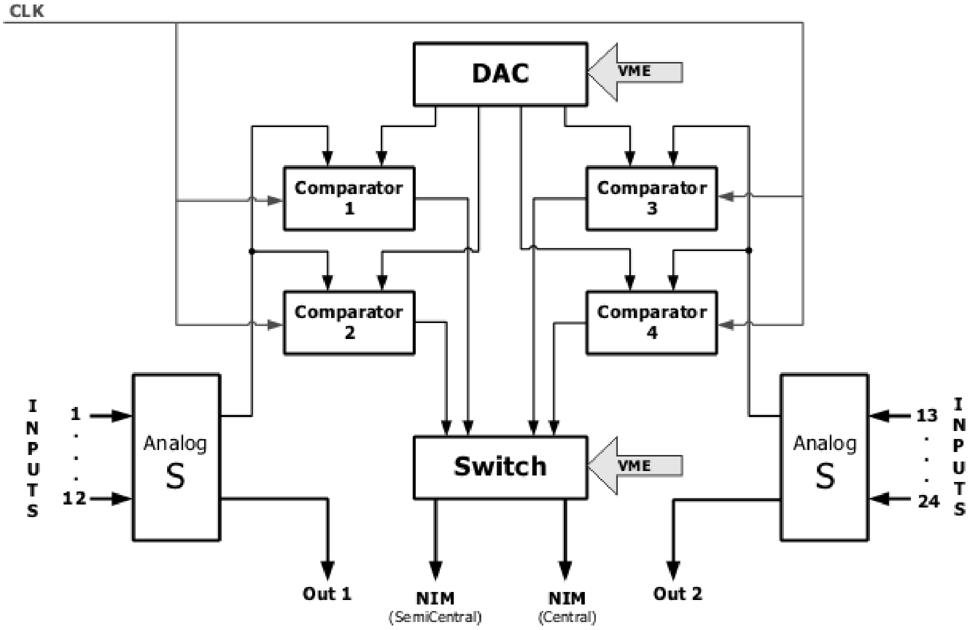

Figure 1.37: Multiplicity Discriminator. S indicates summation unit.

The 12 analogue signals originating either from T0-A or from T0-C arrive at the input of an analogue summator (Σ). The summed–up signals than go to the inputs of the three comparators (D1, D2, D3) and one analogue output. The threshold voltages, set with 8-bit resolution, correspond to the low, middle, and high level of multiplicity. These voltages are shaped by the multi-channel Digital to Analogue Converter (DAC) using the digital octal codes written to the RG1- RG3 data registers, allowing for remote control. After additional stretching, the output signals from the comparators come to the outputs of low (Output1), middle (Output2), and high (Output3) levels of multiplicity.

1.8.5 Mean Timer

Just as the time difference between T0-A and T0-C gives vertex position along the z-axis, the average of T0-A and T0-C arrival times cancels this dependence and yields position-independent collision time (plus some fixed delay along the cables, fast electronics, etc.). On-line calculation of the collision time is accomplished by a time-coordinate compensator (Mean Timer) whose schematic diagram is shown in Fig. 1.38. The prototype of the Mean Timer has been tested in in-beam conditions at CERN during the July 2003 run and yielded consistency of about 10 ps of compensation error, as shown in Fig. 1.39. Since the Mean Timer signal (T0) is extracted from two independent pulses, T0 time resolution is better from that of a single detector by about $\sqrt{2}$. The actual results from the 2003 experiment yielded $\sigma_{T0} = 28\,\text{ps}$.

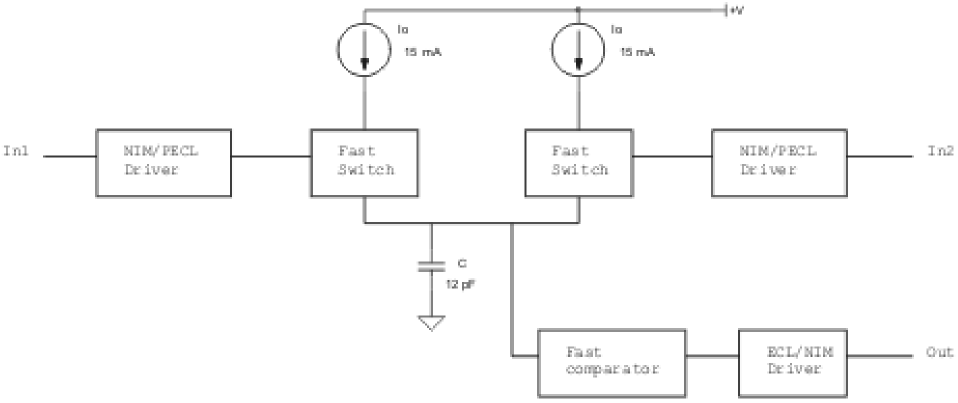

Figure 1.38: Mean Timer. UV1, UV2 are Univibrators (monostable multivibrators); Sw1 and Sw2 indicate switches; GI is a current generator; FC = Fast Comparator; and F is a shaper for forming the output pulses.

1.8.6 Variable Delay Unit

Strict matching of the characteristics of all 24 PMT units forming the T0 detector is simply not possible. As a result each T0 detector tube will operate at a different and individually selected voltage. This alone will cause differences in the arrival times of the signals of up to few ns. To equalize these and comparable differences we have designed the Variable Delay Unit (VDU). Each VDU channel consists of an NIM to ECL converter, an MC100EP195 chip with programmable delay, and an output ECL to NIM converter. A dedicated register connected through an interface with VME is used to record the value of delays. The block diagram of the current prototype VDU is shown in Fig. 1.40.

1.8.7 Charge to Time Converter

T0 will not develop its own readout system but use the one developed for TOF, as explained in the next chapter. The normal procedure to digitize and store the amplitudes of PMT signals would be to use a Charge to Digital Converter (QDC). Although TOF does have provision for a QDC it does not have sufficient resolution to cope with the dynamic range expected from the T0 signals. As the resolution of

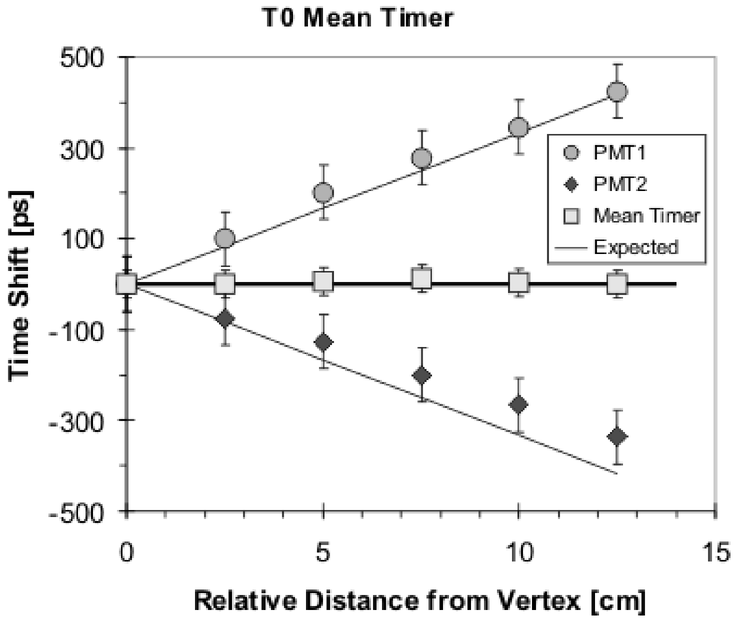

Figure 1.39: Performance of the Mean Timer determined during the July 2003 test run at CERN.

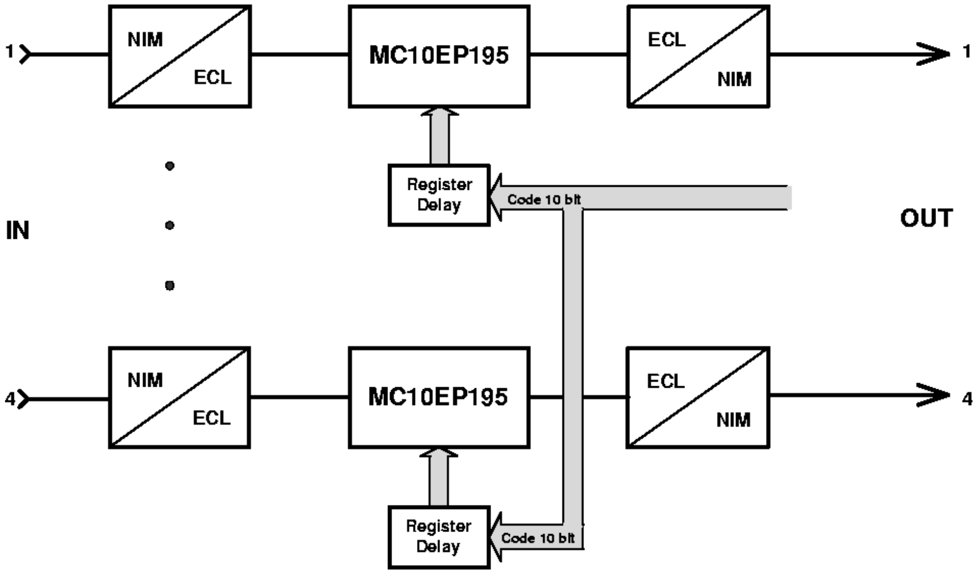

Figure 1.40: Block diagram of prototype VDU.

the TOF TDC is much better it was decided to develop a Charge to Time Converter (QTC) and connect its output to the TOF TDC for digitization, readout and storage. The same approach is used to digitize the summed amplitude used for multiplicity determination. For unification of the measurements and data transmission to the DAQ, HPTDC converters (designed for other ALICE detectors) are used for final charge-to-code conversion. Thus, the QTC converts the amplitude (charge) to the time delay adequate for coding using an HPTDC converter. The logarithmic characteristic of the converter is necessary due to the wide range in the PMT signal amplitude. From the output of the comparator, the signal goes to the differential circuit (Shaper 1 and 2 in Fig. 1.41), generating pulses bound to the rising and falling edges of the comparator pulse. These pulses go to the ECL-LVDS level converter for shaping into the LVDS format.

The first prototype of the QTC unit was successfully tested during the June 2004 experiment at CERN.

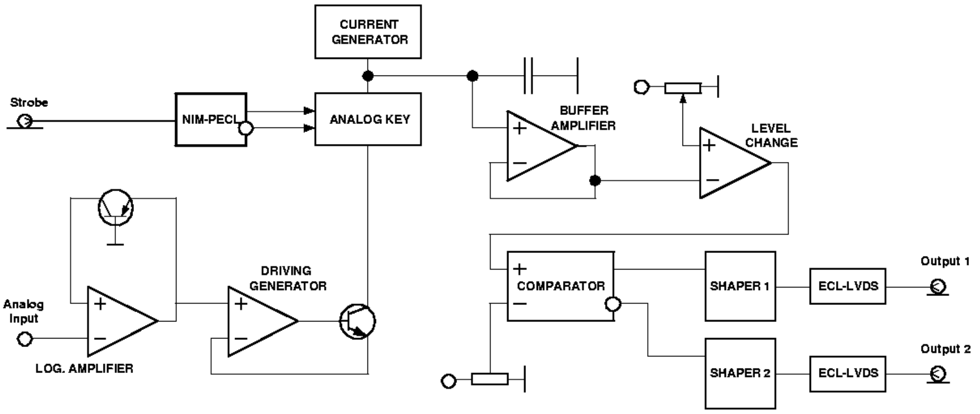

Figure 1.41: Schematic layout of the QTC unit.

1.9 Beam Test of complete T0 system

The beam tests described in Chapter 1.6 were essential to verify the validity of the concept of the detector and to determine the baseline parameters of the main T0 components. Since then progress has been made both in the detector R&D and in the development of the electronics. There have also been important advance in ALICE integration, down to the defining of cables, connectors, etc. With prototypes of all major electronics components, the actual cables, PMTs, and quartz radiators, we have made additional in-beam tests recreating closely the actual ALICE environment. The goal of these tests was to check the detectors and electronics with real signals as opposed to laser and generator pulses in low-noise laboratory conditions and to find out if the baseline parameters (such as the size of the quartz radiators) are indeed the best possible. Two measurements with test beam were held in July 2003 and in June 2004. The first concentrated on the electronics prototypes. During the 2004 session the second generation of prototypes was tested but the main emphasis was on light collection and the pulse shape obtained by various quartz radiators. Otherwise both experiments were very similar so, for the sake of brevity, only the 2004 setup is described.

1.9.1 Experimental Setup

The beam (a mixture of 6 GeV/c negative pions and kaons) that for the purpose of our measurements can be considered as Minimum Ionizing Particles (MIP) as they could easily penetrate all (usually up to four) detectors placed in their path without any nuclear interactions nor appreciable loss of energy. A typical configuration with four T0 detector modules is shown in Fig. 1.42. Usually the first and the last detector worked as triggers while the two middle detectors were investigated. The modules were placed one after the other and were well aligned with the beam axis. The width of the beam was considerably larger than 3 cm - the diameter of the largest tested detector.

Figure 1.42: Photograph of a typical detector configuration during the 2004 test run at CERN PS. There are four PMT + quartz detector units. Each unit has its own aluminum casting with plastic end cups.

Depending on the need, the individual units could be shifted in respect to each other (to change the relative timing), tilted (to reduce the working area and to check the beam profile) or inverted 180° to study the pulse from the particles traversing the radiator in the "wrong direction".

Each PMT divider ended with a short pigtail of cables going to a small patch panel on the supporting rail. To reproduce exactly the expected configuration in ALICE the PMT signals were sent from the patch panel to the shoebox prototype (see Fig. 1.43) over a 6 m long cable. From the shoebox the signals were delivered over 25 m long cables to the main electronics rack, just as it will be in the final setup.

1.9.2 Tested Quartz Radiators

The baseline size of the T0 quartz radiator was 30 mm long (see calculations in Section 1.4.3) and 30 mm in diameter. This diameter coincides with the outer diameter of the PM tube (see Fig. 1.2) but is substantially larger than the diameter of the photocathode (20 mm). Larger cross section of the radiator gives a larger solid angle, increasing the overall detection efficiency. In broad beam conditions and assuming perfect electronics the detection probability can be taken as simply proportional to the cross section of the radiator. The price to pay when the diameter of the radiator exceeds that of the photocathode is the deterioration of the shape of the pulse, leading to the loss of time resolution, and decreased efficiency. The best way to verify the results of simulations is to take real measurements. We tested radiators of 3 diameters (the length of all radiators was 30 mm):

- 30 mm (the current baseline; same as the PMT)
- 20 mm (matching that of the photocathode)
- 26 mm (an arbitrary intermediate value)

From January 2005 the new baseline is 20 mm in diameter and 20 mm long.

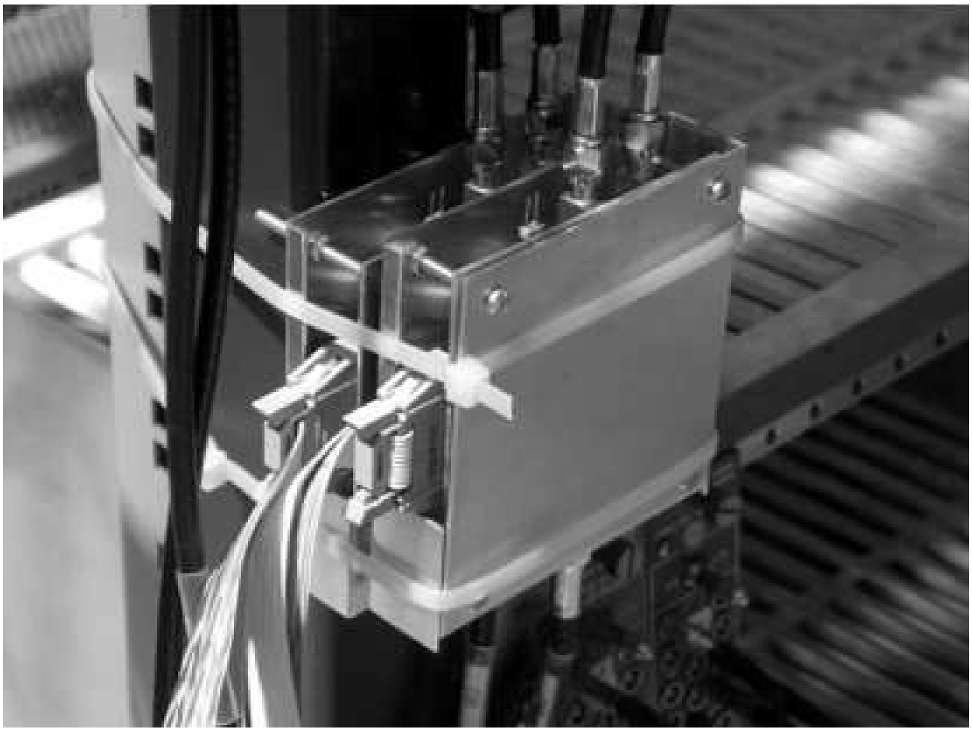

Figure 1.43: Photograph of the shoebox prototype (for two input channels) tested at CERN PS in June 2004. The input cables are seen entering from below and the output cables exit from the top. The ribbon cables deliver ±6 V of power.

Figure 1.44: Test version of the main T0 electronics rack photographed during the 2004 run at CERN.

1.9.3 Time Resolution

The most direct way to determine the time resolution of a detector (σ_{det}) is to use two identical detectors as start and stop and to analyse the collected TOF distribution of mono-energetic particles. Ideally, this would be a Gaussian distribution, therefore:

$$\sigma_{TOF} \approx \frac{\mathrm{FWHM}_{TOF}}{2.35} \tag{1.2}$$

and

$$\sigma_{det} = \frac{\sigma_{TOF}}{\sqrt{2}}\,, \tag{1.3}$$

where TOF stands for Time–Of–Flight, FWHM is full width at half maximum and σ_{det} is the time resolution of the detector (in our case one quartz + PMT Cherenkov module). The ALICE requirement for T0 is

$$\sigma_{det} \leq 50\,\mathrm{ps} \tag{1.4}$$

A typical TOF spectrum obtained during the June 2004 experimental session is shown in Fig. 1.45 and the result for all 3 radiators is summarized in Table 1.6.

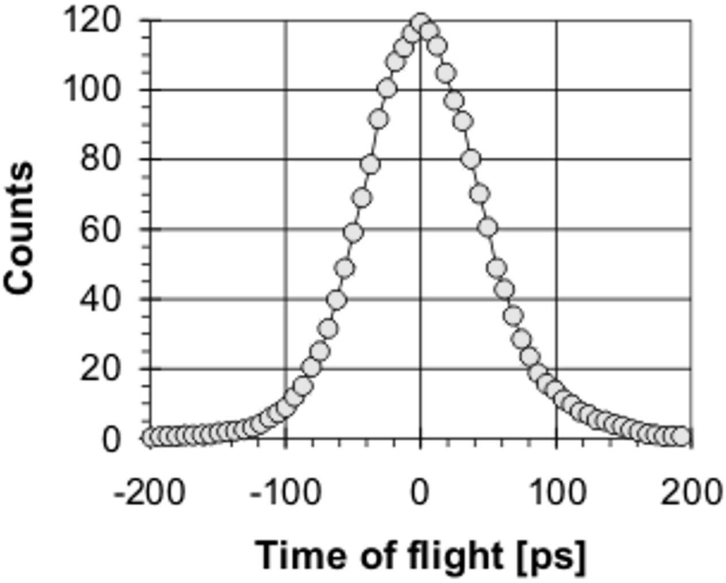

Figure 1.45: Typical TOF spectrum obtained during the 2004 test run at CERN PS. FWHM is 94 ps, which corresponds to $\sigma = 28\,\mathrm{ps}$.

As expected, the best resolution is achieved with the smallest radiator, but even with the current version of the shoebox electronics all results are well within the ALICE specification.

1.9.4 Pulse Shape and Efficiency

Figure 1.46 shows measured amplitudes of the PMT output obtained for 3 different radiator sizes.

The 30 mm diameter radiator produces a broad amplitude spectrum with a characteristic two-hump structure that we have observed before (Fig. 1.20) and is well reproduced by simulations (Fig. 1.23). The lower bump comes from light loss through the area around the photocathode. This gap is smaller for a 26 mm radiator but qualitatively the spectrum is not much different from that of a 30 mm radiator. A great improvement occurs for the smallest radiator i.e., when the diameter does not exceed that of the photocathode. In this case all the light produced inside the volume of the radiator is directed to the

Table 1.6: Dependence of FWHM and time resolution (σ) on the diameter of the Cherenkov radiator. The values in brackets were obtained when the signals were amplified in the shoebox instead of going directly to CFD. Current improvements to the shoebox design should reduce these values, so they are preceded with a less than or equal to sign.

Radiator diameter	**FWHM (TOF)**	**σ (T0detector)**
30 mm	122 ps (≤ 140 ps)	37 ps (≤ 42 ps)
26 mm	112 ps (≤ 128 ps)	34 ps (≤ 39 ps)
20 mm	94 ps (≤ 115 ps)	28 ps (≤ 35 ps)

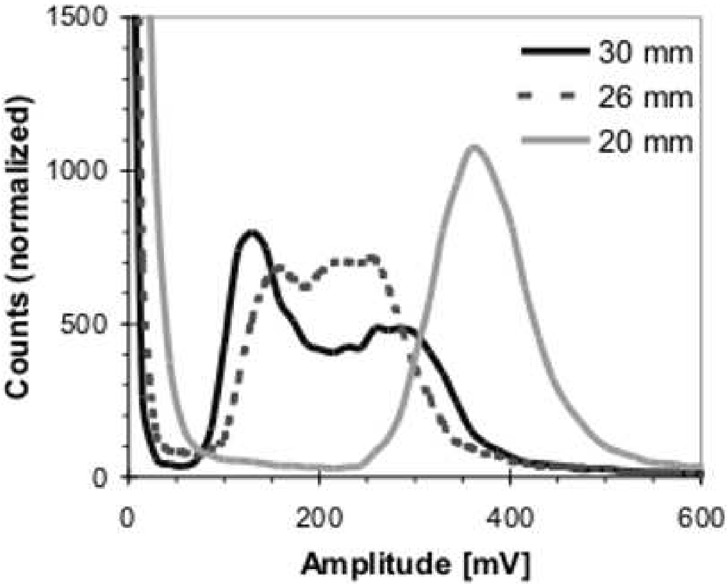

Figure 1.46: Dependence of the light output of a PMT on the diameter of the radiator produced with minimum ionizing particles. 1 MIP results in about 180 photoelectrons ejected from the cathode of the PMT. For easier comparison the spectra were smoothed and their areas normalized.

photocathode. The spectrum shifts up and becomes Gaussian, reflecting the statistical nature of photo conversion. There is a broad and clear area separating the peak from the noise (pedestal) level.

As discussed before, the consequence of the radiator's reduced diameter is the reduction in the covered solid angle (detection efficiency) that is roughly proportional to the second power of the diameter (area). This, however, is true only if the discriminator threshold can be placed at sufficiently low value. A rise in the threshold will lead to loss of efficiency. Figure 1.47 illustrates the dependence of efficiency on the threshold level, calculated using the amplitudes spectra of Fig. 1.46.

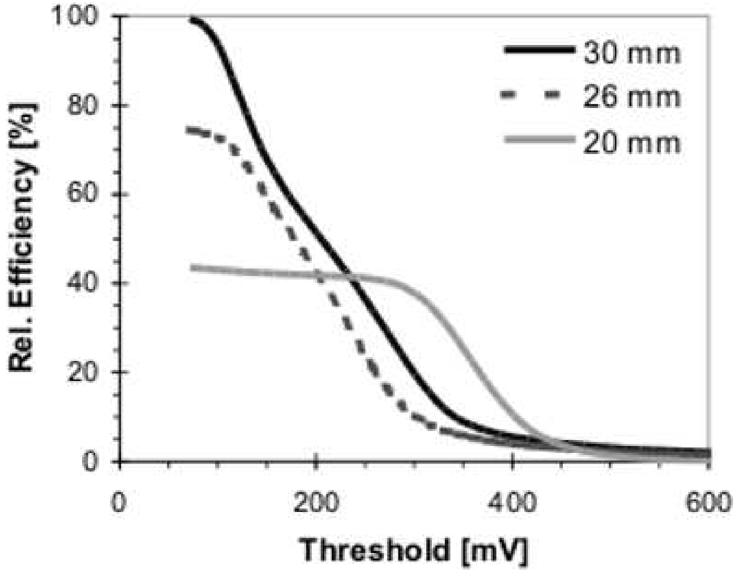

Figure 1.47: Efficiency as a function of the threshold calculated using measured amplitude spectra. 100% was assigned to the 30 mm radiator and the maximum values for the 26 and 20 mm diameter radiators were scaled accordingly.

The steep drop of efficiency for 30 and 26 mm diameter radiators with the increase of the threshold is somewhat disturbing. It means that even if no noise problems prevent the setting of the threshold value sufficiently low, any instability will cause noticeable variations in efficiency. In contrast the characteristics of the 20 mm quartz are excellent with a prominent and broad plateau.

1.9.5 Sensitivity to the Particle Backsplash

Cherenkov radiation is strictly directional but since the polished walls of the quartz radiator work as a mirror, particles travelling in the "wrong" direction will also produce detectable light pulses. This undesirable effect can be partially reduced by covering the front surface of the radiator with a light-absorbing layer, for instance by glueing (to get optical contact) a black paper on top of it. It works well for particles travelling exactly in the opposite direction but those at intermediate angles will inevitably produce some signals. This may not be a problem for T0-C despite being just next to the muon absorber, because the absorber was designed to minimize particle backsplash. This, however, will not be the case for T0-A, which is placed in the proximity of a vacuum pump, valve and support structure. It is therefore important to know what kind of spectra are to be expected from the "wrong" particles. The largest amplitudes from strain particles (the worst-case scenario) arise when they travel in exactly the opposite direction and the front of the radiator is free from optical contact with a light-absorbing material. The results are shown in Fig. 1.48 (26 mm diameter radiator) and Fig. 1.49 (20 mm radiator).

It is reassuring to see that with the 20 mm radiator even the largest signals from strain particle can be effectively (without the loss of pulses from good events) discriminated against by raising the threshold. For 30 and 26 mm radiators this would not be the case.

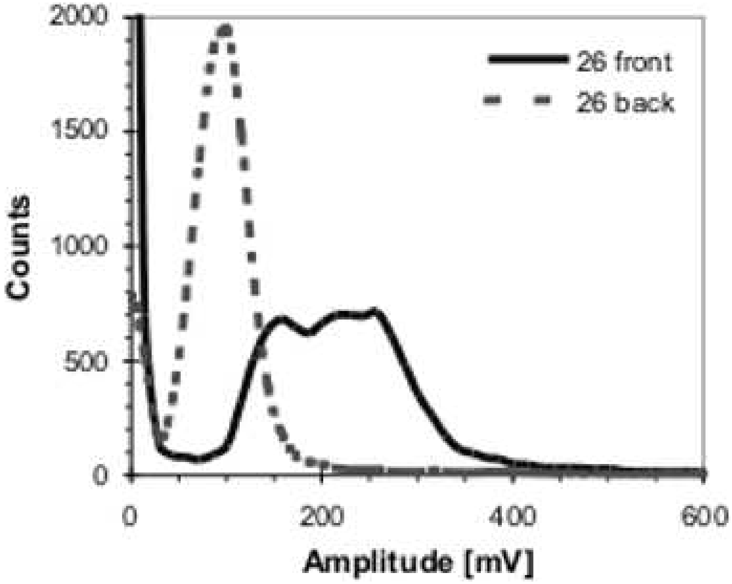

Figure 1.48: Response of the T0 module with 26 mm diameter radiator to MIPs entering directly from the front (solid line) and from the opposite direction (dashed line).

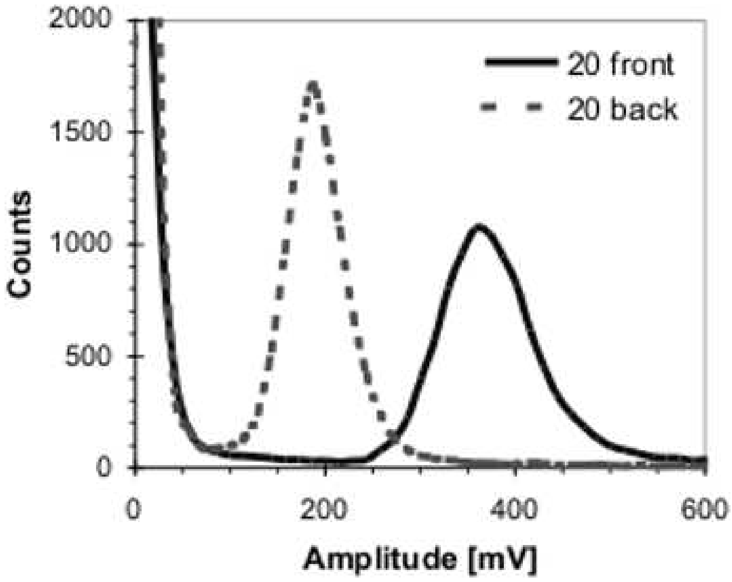

Figure 1.49: Response of the T0 module with 20 mm diameter radiator to MIPs entering directly from the front (solid line) and from the opposite direction (dashed line).

1.9.6 Light Transmission Measurements

The radiators used in our experiments were made at a different time and presumably also from different batches of the quartz material. To check the consistency and quality of production we have made light transmission measurements for each of the tested radiators. The coved wavelength (200–600 nm) matches that of PMT sensitivity. The results are presented in Fig. 1.50. They show that while there are indeed small differences between the samples, the overall quality of quartz radiators is good. The sample with the highest transmission (sample 1) was from the production run of 30 mm diameter radiators.

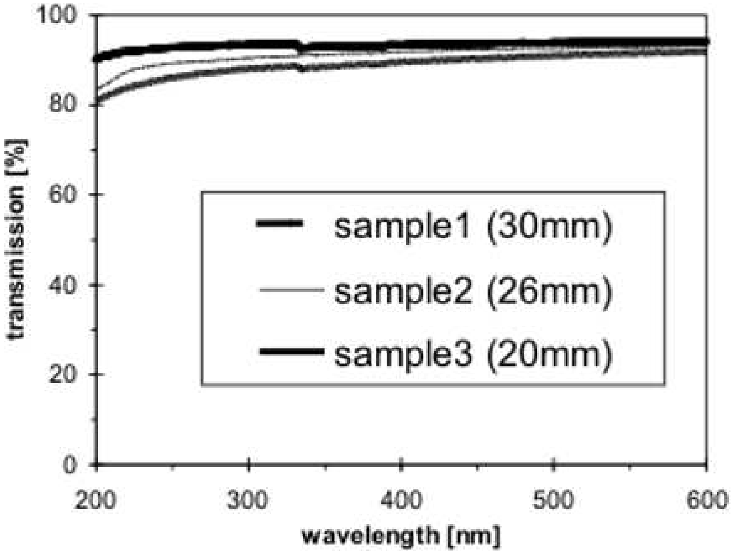

Figure 1.50: Light transmission through 3 cm thick samples of quartz radiators as a function of the wavelength.

1.9.7 Conclusions

The most important conclusion of the beam tests of the complete T0 system is that with the actual cables, connectors and prototypes of the electronics and for all tested radiator types the required time resolution of $\sigma \leq 50\,\text{ps}$ has been achieved.

The tests demonstrated the excellent amplitude spectrum of the 20 mm diameter radiators. It is so much better than the 30 mm radiator that it justifies considering a change in the current baseline. The only drawback would be reduced efficiency in pp collisions. This reduction can however be compensated, if necessary by the doubling the number of T0 modules in the T0-A array, as demonstrated in Table 1.7.

Table 1.7: Simulated efficiency in pp collisions (PYTHIA 6.125; 1000 events) for the baseline configuration (12–12), and for the configuration with 24 detectors on RB24 side (24–12).

Number of detector modules in T0-A	**Number of detector modules in T0-C**	**Efficiency in pp with 30 mm diameter radiators**	**Efficiency in pp with 20 mm diameter radiators**
12	12	53%	36%
24	12	–	49%

1.10 Data Readout

As mentioned in Chapter 1.8, the only ALICE sub-detector requiring non-trigger data from T0 is TOF. TOF needs time and amplitude information from each PMT to make off-line corrections that should further improve the precision and stability in definitions the interaction time. Otherwise, the only reason for storing raw T0 parameters would be for monitoring. Therefore, to cut costs and to guarantee the performance of T0, our readout (see Fig. 1.51) will be nearly identical to that of the TOF detector. For conciseness, only the modifications and changes in the TOF readout will be presented here. Together with arrival times and amplitudes from each PMT a handful of other parameters (vertex, summary amplitudes, etc.) will also be read out and stored by ALICE DAQ in exactly the same fashion. From the point of view of the readout architecture, the T0 detector will be just one more, fully independent, sector of the TOF detector.

The main difference between T0 and TOF pulses (relevant to the readout system) is their dynamic range. To accommodate the larger amplitude range from T0 a QTC + TDC will be used instead of QDC (see Section 1.8.7). A more serious problem is the range of the TDC. The High Performance TDC (HPTDC) developed by TOF has a range of about 200 ns, nearly one order of magnitude more than what is needed by T0. The resolution will be naturally sufficient but there is a problem with the dead time.

There is a small (below a few percent) probability that the same T0 module will produce a pulse in two consecutive bunch crossings. In pp collisions they are separated by just 25 ns. The first pulse will start the HPTDC and block it for the next 200 ns preventing the conversion, readout and storage of the second pulse. Let's further assume that the first signal was just a noise, a strain particle or a cosmic ray while the second come from proper interaction that should be triggered and stored. In this possible but unlikely case the T0 will produce all the correct trigger signals but the data (time and amplitude) from that particular PMT will not be digitised.

There are several ways to handle this problem. The easiest is to simply ignore such events and require the absence of T0 data for at least 200 ns prior to the valid interaction. The only drawback would be a slight (below a few percent) reduction in the data-taking rate. This is the solution that we prefer and consider as the baseline, since it has no consequence for Pb–Pb running and very small effect for pp.

The second solution is to use the the T0 Vertex signal as a strobe for the T0 readout. In this way no reduction in the data-taking rate will take place but the information on the T0 operation in non–trigger conditions will be absent. Such a solution would also require additional delays to the time and amplitude signals in waiting for the production of T0 Vertex. Such delays would slightly worsen signal quality.

Finally, it is possible to solve the problem completely by demultiplexing the signals from each PMT into 16 TDC inputs instead of just one. The prototype of such a demultiplexer has been built and successfully tested (see Fig. 1.52). It may be used as the base for production modules. The biggest disadvantage of the demultiplexer solution is a 16 fold increase in readout electronics. For that reason we consider it only as an upgrade option.

1.10.1 Data Readout Module (DRM)

Each crate will be equipped with a Data Readout Module (DRM) card that will act as the main interface between the Central ALICE DAQ, the CTP and T0 electronics (see Fig. 1.53). The DRM will receive and distribute the 40 MHz clock and the trigger signals (L1 and L2) to the T0–TRMs. The clock will be received through an optical fibre, while the other signals will be derived from a TTCrx. The clock will be distributed to T0–TRM and fast electronics in LVDS standard. The control signals (L1, L2 accept and L2 reject) will be distributed with an LVDS bus to the T0–TRMs through an external flat cable.

The DRM will read the data from the T0–TRM modules. If an L2 reject is received the corresponding event buffer will be cleared on the T0–TRMs, otherwise, on L2 accept, data will be transferred from all the T0–TRMs to the DRM via the VME64 backplane. This data transfer is performed by the FPGA.

The data will be further processed and encoded by a DSP on board and sent through a standard

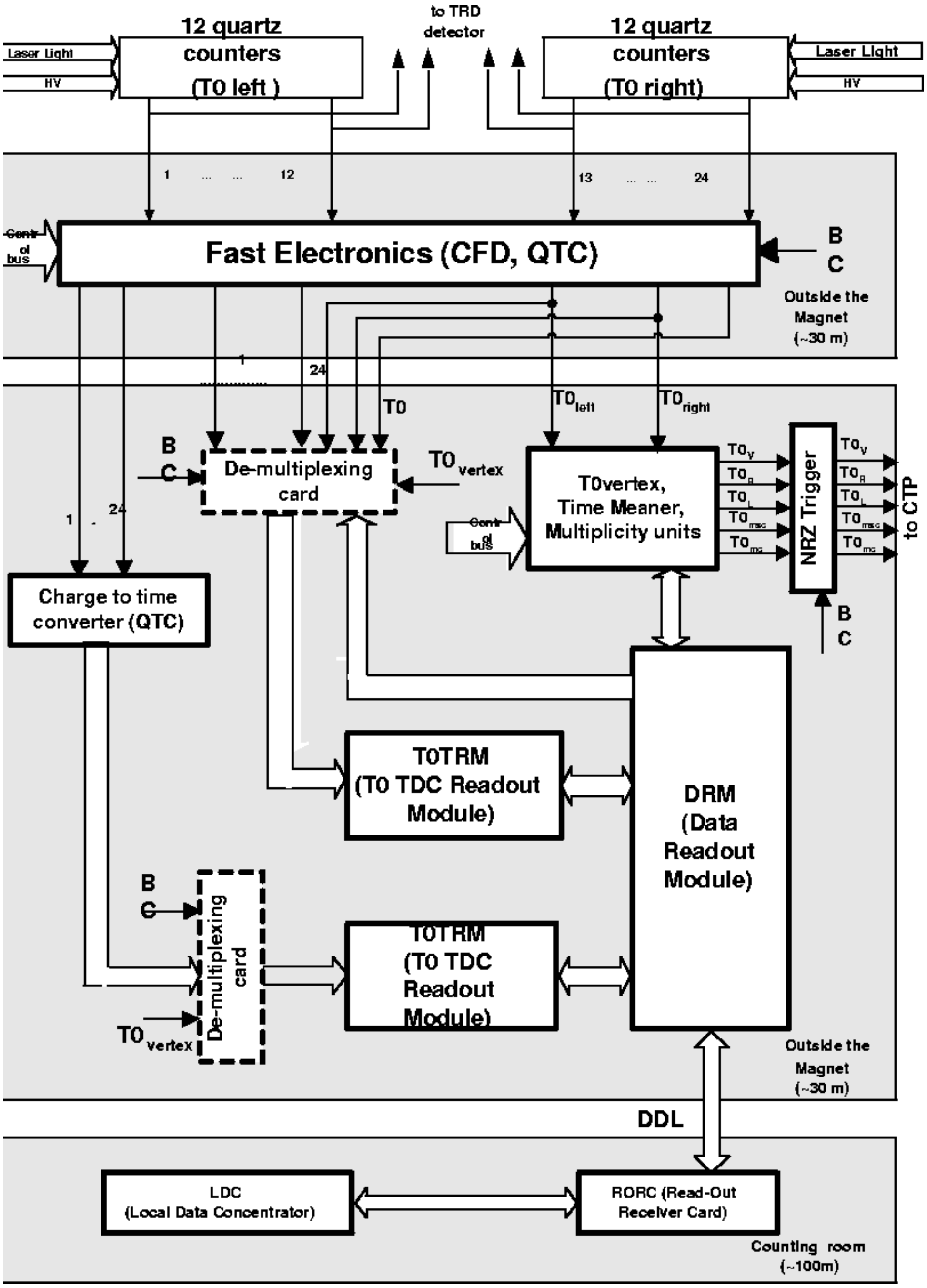

Figure 1.51: Block diagram of T0 readout.

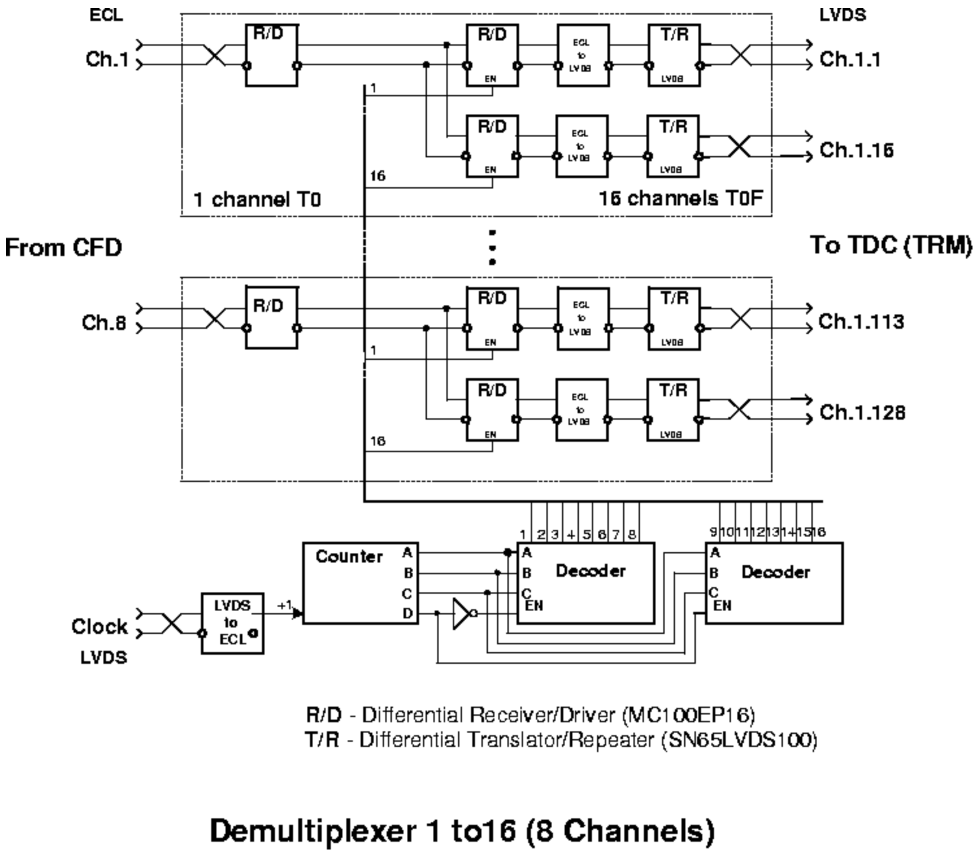

Figure 1.52: Block diagram of the demultiplexer.

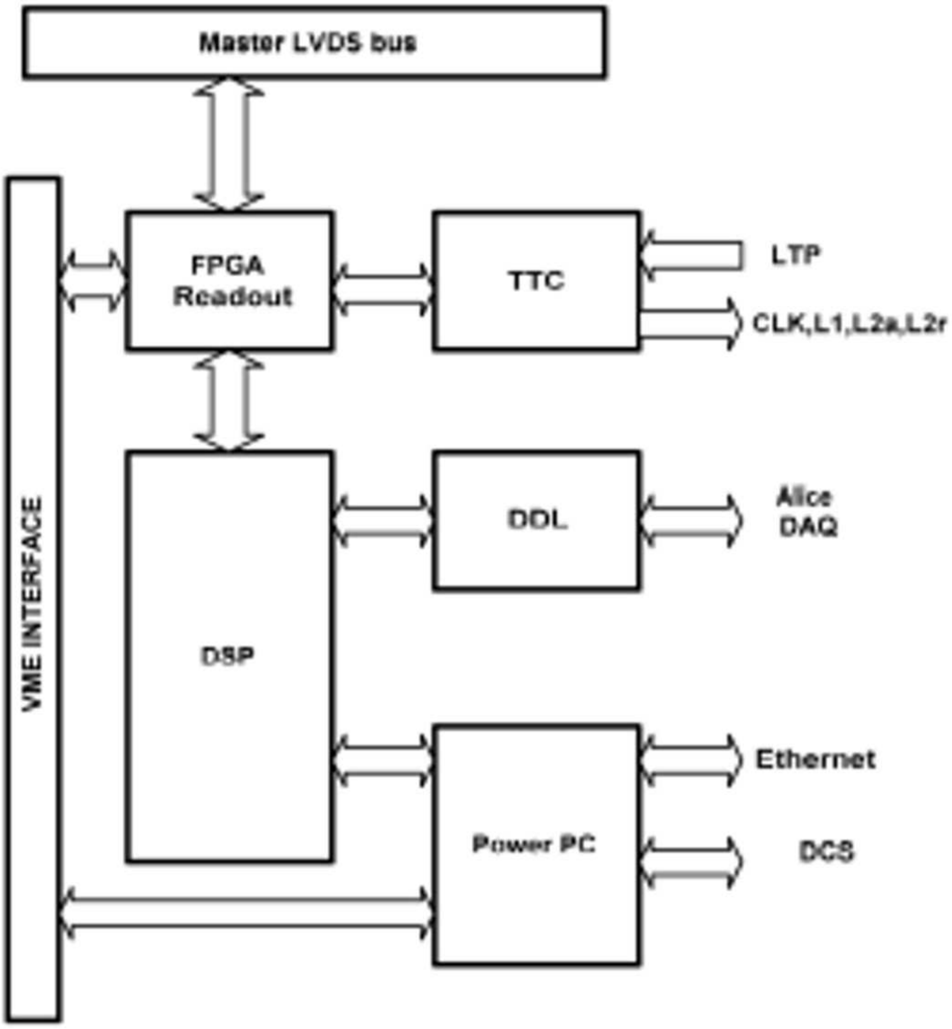

Figure 1.53: T0 Data Readout Module.

ALICE DDL interface to the central DAQ. A power PC will allow monitoring of the data and will host the slow controls of the T0 system (threshold setting, delay setting etc.). All these I/O devices (TTC and DDL interfaces and power PC cards) will be developed as a piggy-back card in standard PMC format applied to a VME card.

1.10.2 TDC Readout Module - TRM unit

An FPGA will perform the readout of the HPTDCs. To ensure high bandwidth the FPGA will act as an external readout controller of two separate chains consisting of 15 HPTDC slaves (in token - base parallel-readout configuration). The use of an Actel Pro Asic Plus FPGA is foreseen. A Digital Signal Processor (DSP) will control various setup operations (including R-C delay chain calibration) and data packaging. The use of an Analog Devices Shark family DSP is foreseen. Memory (RAM and SRAM) is provided for event buffering and program hosting.

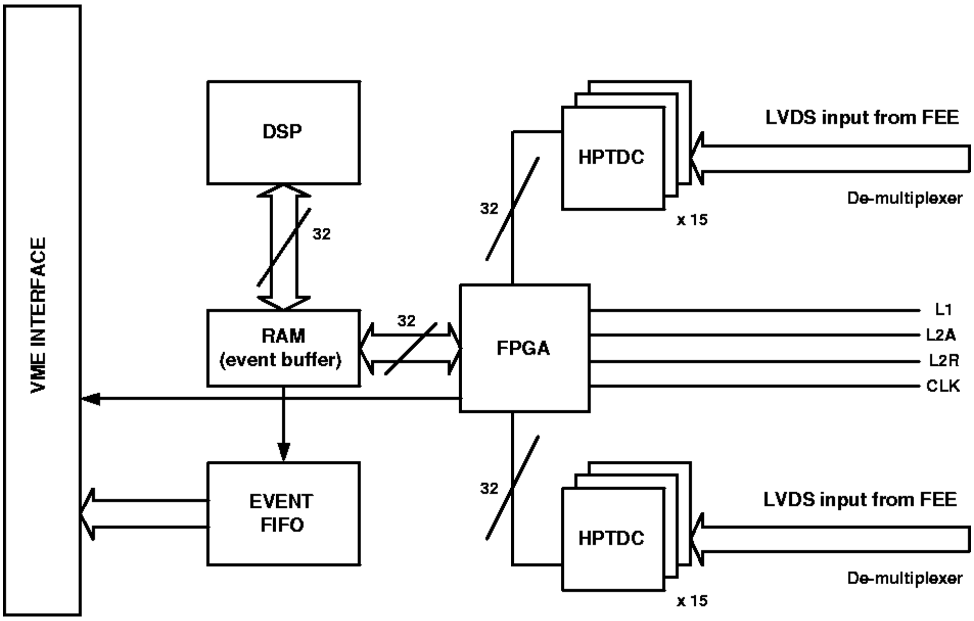

Figure 1.54: TRM unit.

Program loading and general control of the TRM will be managed through a VME interface (see Fig. 1.54). Initialization and setup of the HPTDC chips will be normally performed through the DSP. At reception of an L1 signal from the ALICE Central Trigger Processor (CTP) the HPTDCs will look for hits with a time offset of $6.2\,\mu$s, moving then to the internal readout FIFO. This operation does not cause dead time to the acquisition of data by the HPTDC.

1.11 Detector Control System

The T0 detector modules are relatively straightforward, stable, and reliable units making controlling them easier. Standard off-the-shelf products will be used as High Voltage and current monitoring devices. The only problems arise from stray magnetic fields in the vicinity of L3 magnet and elevated radiation levels. This, however, is a common problem for all ALICE detectors. We are simply planning to use one of the C.A.E.N standard solutions. There are also several ready-made solutions for the control of electronics. In each T0 channel there are several thresholds, delays, etc. that have to be adjusted prior to and sometimes during the run. T0 Vertex and Multiplicity Units control the main trigger signals and need to be addressed during normal ALICE operations. Monitoring of all PMT modules will be done with laser pulses during the longer breaks in the beam. This should cause no problems as even the current laser power supply has the provision for remote triggering.

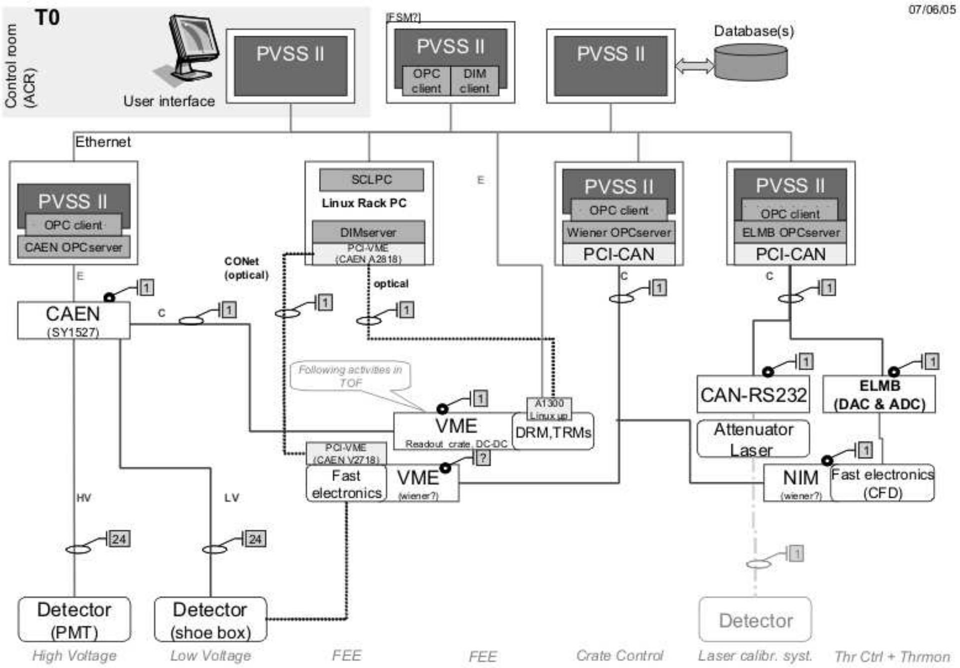

Figure 1.55: Scheme of T0 DCS.

The DCS scheme for the T0 detector is shown in Fig. 1.55. The main sub-systems are high voltage (HV), low voltage (LV), settings threshold and delays, laser control, generator control and T0–TDCs and T0–DRM readout cards. The list of signals to be monitored and controlled for the T0 detector is listed in Table 1.8.

The T0 electronics will be located in two different areas: the shoebox will be placed inside the magnet (these regions can be accessed only during a long shutdown), fast electronics and T0 TDC/DRM cards will be in the crates just outside the L3 and can be accessed even during a short shutdown. The High and Low Voltage to the PMTs and electronics will be provided by a CAEN SY2527 system with high and low voltage boards. A CAEN OPC server will interface the crate with PVSS, through Ethernet.

The connections between the control computer and the VME crates with fast electronics will be based on a CAEN V2718-A2818 VME-PCI optical link bridge. The module V2718 is a 1-unit wide 6U VME master module, which can be interfaced to the CONET (Chainable Optical NETwork) and controlled by a standard PC equipped with the PCI card CAEN module A2818. The T0–TRM and T0–DRM are presently under development by the ALICE TOF group and we shall use their solution.

For fast electronics we shall use standard VME crates. The control and monitoring will be via CANbus and Kvaser CAN interface card. The top-level application will be a SCADA system based on PVSS software that communicates with the hardware via OPC or DIM servers. Support for all equipment will be implemented based on the JCOP framework.

1.12 Organization

1.12.1 Participating Institutes

The main institutes participating in the design, construction and operation of the T0 detector are:

- HIP — University of Jyväskylä, Department of Physics and Helsinki Institute of Physics, Jyväskylä, Finland;

Table 1.8: Main parameters of the Detector Control System for the T0.

Subsystem	location	Controlled parameters	Number	Parameter	Control
Fast electr.	VME	delays Thresholds and walks for CFD Thresholds for T0-v Thresholds for multiplicity trigger	24 24 2 - 3	- voltage voltage - voltage	- W R/W - R/W
T0-TRM	VME crate	same as TOF			
T0-DRM	VME crate	same as TOF			
Low voltage for Shoebox	CAEN 1527	LV supply on/off LV settings and readings safety switch	24 24 1	voltage complex voltage	R/W R/W on/off
HV voltage	-	HV supply on/off HV settings and readings safety switch	24 24 1	voltage complex voltage	R/W R/W on/off
Laser system	-	switch attenuator	1 1	- complex	on/off R/W
Generator	-	switch	1	voltage	on/off

  - Wladyslaw Trzaska (Project Leader)
  - Sergey Iamaletdinov (Graduate Student)
  - Vladimir Lyapin (Shoebox, LCS)
  - Tomasz Malkiewicz (Graduate Student, Database)

- MEPhI - Moscow Engineering Physics Institute, Moscow, Russia
  - Vladislav Grigoriev (Leader of the Russian Team)
  - Vladimir Kaplin (Electronics)
  - Alexandr Karakash (PMT, test measurements)
  - Vitaly Loginov (Electronics)
- INR — Academy of Science, Institute of Nuclear Research, Moscow, Russia
  - Alexei Kurepin (INR Group Leader)
  - Fedor Guber (Mechanics)
  - Tatyana Karavicheva (DCS, readout)
  - Oleg Karavichev (Electronics)
  - Victor Marin (CFD)
  - Alla Mayevskaya (Simulations)
  - Andrei Reshetin (PMT shielding)
- KI — Russian Research Center “Kurchatov Institute”, Moscow, Russia
  - Evgeni Meleshko (T0 Vertex, Multiplicity)
  - Anatoly Klimov (Technical Project)

- WAU — Warsaw University of Technology, Faculty of Physics, Warsaw, Poland
  - Radomir Kupczak (DCS, readout)
  - Wiktor Peryt

The Greek group from Athens (Marta Spyropoulu-Stasinakhi) has also expressed serious interest in participating in the T0 DAQ. The Greek group would contribute both in terms of manpower and core costs.

1.12.2 Cost Estimate and Resources

During the signing of the Memorandum of Understanding the T0 project as such did not yet exist. It evolved later by dividing the initial FMD into T0, V0 and the current FMD (based on silicon detectors). It is therefore still unclear how much core money can be used by T0. The only currently available cash comes from part of the Finnish Core Contribution. At the start of the project it was 200 kCHF. This was estimated roughly sufficient for the detector modules, mechanics and front-end electronics. By the end of 2004 more than half of that sum will have been spent. To complete the entire project additional funds will be needed. The main uncertainty is the cost of readout modules. They are custom made by the TOF collaboration and do not have a clear price tag. The final price of the High and Low Voltage power supply systems is also unclear. Systems like the new (not yet on the market) C.A.E.N. EASY are expensive but the cost per channel can be substantially reduced if shared with another subdetector. We are exploring such possibilities. All in all the total cost of T0 should be of the order of 400 kCHF.

1.12.3 Commissioning

T0 is a small detector giving some degree of flexibility in defining and meeting internal milestones. There are, however, issues where no delays are permitted. In August 2006 installation of the detectors on RB26 will start and T0-C will be the first detector installed. This is the most important milestone because after the installation T0-C shall remain practically inaccessible until the end of the operation of ALICE (see the chapter on integration). Therefore it is of utmost importance to ensure the quality and reliability of all parts of T0-C. All the other components of T0, even those inside the L3 magnet (T0-A and the shoeboxes) will have reasonable accessibility, allowing for modification and replacement even during short shutdown periods. In light of this perfection of the detector modules is in the highest priority for us until August 2006. By the end of 2005 T0-C and T0-A will be pre-assembled and tested in Finland prior to their shipment to CERN. Once at CERN both T0 arrays will be tested again. The test will be repeated once more after installation.

Naturally, work on electronics, readout and DCS proceeds in parallel. For instance, completion of the shoeboxes is also of high priority as it involves collaboration between several groups (T0, V0, TRD). Right now (August 2004) the prototypes of all major electronics component have been built, fully tested and proven to work well. In principle, we should be ready to change from the prototypes to the production modules. This, however, is unlikely to happen before the end of 2005 as we are also investigating the possibility of finding some common electronics solutions with V0 and further integration with TOF. For instance we are waiting to test the latest version of the NINO chip (developed by TOF). In the event of positive results the use of a joint TOF, V0 and T0 standard would greatly simplify and accelerate our work.

The first batch of the production components for the laser system have already been ordered. One more series of test is foreseen before the full system will be purchased. If no problems arise, the laser calibration system should be complete in time for the pre-shipment tests of T0 at the end of 2005.

1.12.4 Safety Aspects

With the exception of the high voltage (1–2 kV) delivered to each of the 24 PM tubes using standard HV cables and SHV connectors, the T0 detector poses no safety hazards.

References

Chapter 1

[1] N. Ahmad *et al.*, ALICE: Technical proposal for A Large Ion Collider Experiment at the CERN LHC, CERN/LHCC-95-71 LHCC/P-3, (1995).

[2] L. Betev and P. Chochula, Definition of the ALICE Coordinate System and Basic Rules for Sub-detector Components Numbering ALICE note ALICE-INT-2003-038, (2003).

[3] S. Beolè *et al.* [ALICE Collaboration], ALICE technical design report of the detector for high momentum PID, CERN-LHCC-98-19, ALICE TDR 1, (1998).

[4] G. Dellacasa *et al.* [ALICE Collaboration], ALICE technical design report of the photon spectrometer (PHOS), CERN-LHCC-99-4, ALICE TDR 2, (1999).

[5] G. Dellacasa *et al.* [ALICE Collaboration], ALICE technical design report of the zero degree calorimeter (ZDC), CERN-LHCC-99-5, ALICE TDR 3, (1999).

[6] G. Dellacasa *et al.* [ALICE Collaboration], ALICE technical design report of the inner tracking system (ITS), CERN-LHCC-99-12, ALICE TDR 4, (1999).

[7] G. Dellacasa *et al.* [ALICE Collaboration], ALICE technical design report of the dimuon forward spectrometer, CERN-LHCC-99-22, ALICE TDR 5, (1999).

[8] G. Dellacasa *et al.* [ALICE Collaboration], ALICE technical design report: Photon multiplicity detector (PMD), CERN-LHCC-99-32, ALICE TDR 6, (1999).

[9] G. Dellacasa *et al.* [ALICE Collaboration], ALICE technical design report: Time projection chamber (TPC), CERN-LHCC-2000-01, ALICE TDR 7, (2000).

[10] G. Dellacasa *et al.* [ALICE Collaboration], ALICE technical design report of the time of flight system (TOF), CERN-LHCC-2000-12, ALICE TDR 8, (2000).

[11] P. Cortese *et al.* [ALICE Collaboration], ALICE technical design report of the transition radiator detector (TRD), CERN-LHCC-2001-21, ALICE TDR 9, (2001).

[12] P. Cortese *et al.* [ALICE Collaboration], ALICE technical design report: Trigger, Data Acquisition, High Level Trigger, Control System, CERN-LHCC-2003-062, ALICE TDR 010, (2004).

[13] P. Cortese *et al.* [ALICE Collaboration], ALICE Physics Performance Report, Volume I CERN-LHCC-2003-049, (2003).

Chapter 1

[1] ALICE Collaboration, Technical Proposal CERN/LHCC/95-71.

[2] L. Betev *et al.*, Internal note, ALICE-INT-2003-038.

[3] L. Betev *et al.*, Internal note, ALICE-INT-2003-039.

[4] A.E. Antropov *et al.*, Nucl. Phys. **B78** (1999) 416.

[5] M. Bondila *et al.*, Nucl. Instrum. Methods Phys. Res. **A478** (2002) 220.

[6] K. Ikematsu, *et al.*, Nucl. Instrum. Methods Phys. Res. **A411** (1998),238.

[7] S. Ahmad, *et al.*, Nucl. Instrum. and Methods Phys. Res. **A387** (1997), p. 43.

[8] S. Ahmad, *et al.*, Nucl. Instrum. and Methods Phys. Res. **A400** (1997),149.

[9] V.A. Kaplin, *et al.*, Beam tests of the first prototype of a Cherenkov counter for ALICE T0 detector. ALICE INT 2000 05.

[10] V.A. Kaplin, *et al.*, Status of the ALICE T0 detector based on Cherenkov counters. ALICE/01–07/ Internal note/T0/ 16 January 2001.

[11] V.A. Grigorev, *et al.*, Nuclear Experimental Techniques, **43 6** (2000), 28.

[12] `http://www.ozoptics.com/` .

[13] `http://www.phillipsscientific.com/phisci1.htm/` .

Chapter ??

[1] B. Rapp, thesis, Production de Dimuons en reactions p–p et Pb–Pb avec ALICE : le detecteur V0 et les resonances de basse masse, Lyon University, June 2004.

[2] B. Cheynis *et al.*, Internal note, ALICE/2000-29 (2000).

[3] ALICE Physics Performance Report, CERN/LHCC 2003-049, ALICE PPR Volume 1 (2003).

[4] B. Cheynis *et al.*, Internal note, ALICE/2003-40 (2003).

[5] T. Sjöstrand *et al.*, Comput. Phys. Commun. **135** (2001) 238 (LU TP 00-30, hep-ph/0010017).

[6] X. Wang and M. Gyulassy, Phys. Rev. **D44** (1991) 3501.

[7] I. Azhgirey *et al.*, LHC Project Note 258 (2001); LHC Project Note 273.

[8] E. Cuautle, G.Paic, and R. Alfaro, Internal note, ALICE-INT-2004-021 (2004).

[9] S. Kim *et al.*, Nucl. Instrum. Methods Phys. Res. **A306** (1995) 206.

[10] STAR collaboration IUCF, Proposal to construct an endcap electromagnetic calorimeter for spin physics at STAR, Internal Report (2002).

[11] BICRON, Saint-Gobain Industrial Ceramics, P.O. Box 3093, 3760 DB Soest, The Netherlands.

[12] KURARAY Corp., 3-10, 2-Chome, Nihonbashi, Chuo-ku, Tokyo, Japan.

[13] HAMAMATSU Photonics, 360 Foothill Rd Bridgewater, NJ 08807, USA.

[14] F. Anghinolfi *et al.*, NINO, an ultra-fast, low power, front-end amplifier discriminator for the time-of-line detector in ALICE experiment.

[15] M. Mota, J. Christiansen, HPTDC, High Performance Time to Digital Converter, version 2.2, for HPTDC 1.3, Proc. ICECS98, Lisbon, 1998, IEEE, Vol 1, p 409.

[16] O. Villalobos Baillie, D. Swoboda and P. VandeVyre, ALICE/98-23, Internal Note. Data Acquisition, Control and trigger: Common report for the preparation of the ALICE technical Design reports.

[17] CAEN, Via Vetraia, 11, 55043 Viareggio, Italy.

Chapter ??

[1] B.B. Back *et al.* [PHOBOS Collaboration], Nucl. Instrum. Methods Phys. Res. **A499** (2003) 603.

[2] H.A. Gustafsson *et al.*, Phys. Rev. Lett. **52** (1984) 1590.

[3] M. Poskanzer and S. A. Voloshin, Phys. Rev. C**58** (1998) 1671.

[4] J.Y. Ollitrault, Phys. Rev. D**46** (1992) 229.

[5] J.Y. Ollitrault, Phys. Rev. D**48** (1993) 1132.

[6] R. Raniwala, S. Raniwala, and Y.P.Viyogi, ALICE-INT-1999-32.

[7] A. Morsch and B. Pastirčák, Internal Note, ALICE-INT-2002-28 version 1.0, (2004).

[8] J.-L. Agram *et al.*, Nucl. Instrum. Methods Phys. Res. **A517** (2004) 77.

[9] Ideas ASA, `VA1_prime2`,
`http://www.ideas.no/products/ASICs/VAfamily.html` .

[10] R. Esteve Bosch, A. Jimenez de Parga, B. Mota and L. Musa, IEEE Trans. Nucl. Sci. **50** (2003) 2460.

[11] R. Esteve Bosch *et al.*, Proc. 8th Workshop on Electronics for LHC Experiments, Colmar 9–13 September 2002.

[12] A. Yokoyama *et al.*, IEEE Trans. Nucl. Sci. **48** (2001) 440.

[13] Ideas ASA, "`VA1_ALICE`",
Draft document, see `http://fmd.nbi.dk/fmd/VA1-ALICE-draft-v1r2.pdf` .

[14] `http://ep-ed-alice-tpc.web.cern.ch/ep-ed-alice-tpc/testing.htm` .

[15] M. Adamczyk *et al.* [BRAHMS Collaboration], Nucl. Instrum. Methods Phys. Res. **A499** (2003) 437.